$D\pm$–K^0_S femtoscopy in pp collisions at $\sqrt{s} = 13.6$ TeV with Run 3 data

Zhihe Han

Central China Normal University (CCNU)

Supervisors: Fabrizio Grosa, Laura Serksnyte

August 19, 2026

Abstract

Abstract. In this note, the measurement of femtoscopic correlations between $D^{\pm}$ and K^0_S mesons in pp collisions at $\sqrt{s} = 13.6$ TeV, using the data collected by ALICE during LHC Run 3, is presented. The measurement probes the strong interaction between D mesons and kaons, providing key experimental input for the determination of the internal structure of the $D^*_{s0}(2317)$ exotic state. The $D^{\pm}$ mesons are reconstructed via the $D^{\pm} \to \pi^{\pm}K^{\mp}\pi^{\pm}$ decay channel, with a machine-learning based selection, and the K^0_S mesons via the $K^0_S \to \pi^+\pi^-$ decay channel, exploiting the characteristic V0 topology. The correlation functions are corrected for the minijet background with PYTHIA8 simulations, and the emitting source is modelled within the core–halo picture. For the first time, known resonances, the $D^*_{s2}(2573)^+$ and the $D_{s1}(2536)^+$, are identified in a charm–strange femtoscopic correlation function, providing an important internal cross-check of the analysis.

1 Introduction

Understanding the strong interaction between hadrons from first principles is one of the central challenges of modern physics. The strong interaction is described by quantum chromodynamics (QCD) [1–3], whose fundamental degrees of freedom are quarks and gluons. QCD is characterised by two key properties: asymptotic freedom and colour confinement. At high energies the strong coupling constant is small, perturbative QCD applies and theoretical calculations agree remarkably well with experimental measurements. In the low-energy regime, in contrast, the coupling becomes large and QCD is strongly non-perturbative: quarks and gluons are confined inside hadrons and can never be observed as free particles. Hadrons are therefore the natural carriers of low-energy QCD physics, and the study of their properties and of their mutual interactions provides a unique window into the non-perturbative regime of the theory.

The constituent-quark model [4, 5], proposed in 1964, successfully classified all hadrons known at that time in terms of mesons (quark–antiquark pairs) and baryons (three quarks). QCD itself, however, does not forbid more complex configurations, such as multiquark states, glueballs or hybrids.

Since the discovery of the $\chi_{c1}(3872)$ (formerly X(3872)) by the Belle Collaboration [6], a growing number of states that cannot be accommodated in the conventional quark–antiquark or three-quark picture has been observed, including the $Z_c(3900)$ [7], the charmed–strange mesons $\mathrm{D}_{s0}^{*}(2317)$ and $D_{s1}(2460)$, the hidden-charm pentaquark states $P_c(4312)^+$, $P_c(4440)^+$ and $P_c(4457)^+$ [9], and the doubly charmed tetraquark $T_{cc}^{+}(3875)$ [10]. These so-called exotic hadrons can be interpreted either as compact multiquark states or as loosely bound hadronic molecules, and discriminating between these two pictures is one of the most fervent discussions in hadron physics [11].

The $\mathrm{D}_{s0}^{*}(2317)$ meson, discovered by the BaBar Collaboration in 2003 in $D_s^+\pi^0$ decays [8], is among the most emblematic candidates. In the constituent-quark model, the mass of the 0^+ P-wave state of the $\bar{c}s$ system is expected around 2.48 GeV/c^2, in strong disagreement with the measured value of 2317.8 ± 0.5 MeV/c^2, which lies about 45 MeV/c^2 below the DK threshold. The most supported interpretation of this mass anomaly is that $\mathrm{D}_{s0}^{*}(2317)$ is a hadronic molecule: a loosely bound state of a D meson and a kaon held together by the strong interaction [11]. If this picture holds, the DK interaction in the near-threshold region should be strongly attractive, and $\mathrm{D}_{s0}^{*}(2317)$ would be its most direct manifestation. Despite being known for more than two decades, however, no decisive experimental evidence for or against the molecular interpretation exists to date. The crucial missing ingredient is direct experimental information on the D–K interaction, which is precisely what would allow the two scenarios to be disentangled.

In this context, femtoscopy [12–14] has become a powerful experimental tool to access hadron–hadron interactions that cannot be probed otherwise. The technique is based on the measurement of the two-particle momentum correlation function $C(k^*)$, where k^* is the relative momentum of the pair in its rest frame. At low k^*, the correlation function encodes both the space–time extent of the particle-emitting source and the final-state interaction between the two particles. For a pair of non-identical particles, $C(k^*)$ is related to the source function $S(\vec{r}^{\,*})$ and to the two-particle wave function $\Psi(\vec{k}^{\,*}, \vec{r}^{\,*})$ by the Koonin–Pratt equation [12, 13]

$$C(k^*) = \int \mathrm{d}^3 r^* \; S(\vec{r}^{\,*}) \; \left|\Psi(\vec{k}^{\,*}, \vec{r}^{\,*})\right|^2 , \tag{1}$$

where $\vec{r}^{\,*}$ is the relative distance of the two particles in the pair rest frame, $S(\vec{r}^{\,*})$ describes the spatial distribution of the emitting source, and Ψ is the two-particle wave function, which includes the strong and Coulomb interactions (and quantum-statistical effects for identical particles). In the case of the $\mathrm{D}^{\pm}$–$\mathrm{K}_{\mathrm{S}}^{0}$ pairs studied in this note, the $\mathrm{K}_{\mathrm{S}}^{0}$ is electrically neutral, so that no Coulomb interaction is present between the two particles and the wave function accounts for the strong interaction only. The strong interaction leaves a characteristic attractive or repulsive imprint on $C(k^*)$ at low k^*, from which interaction parameters such as the scattering length and the effective range can be extracted. A schematic illustration of the correlation function in different scenarios, showing the quantum-statistical effects (Bose–Einstein enhancement or Fermi–Dirac suppression) and the imprint of the strong interaction, is shown in Fig. 1.

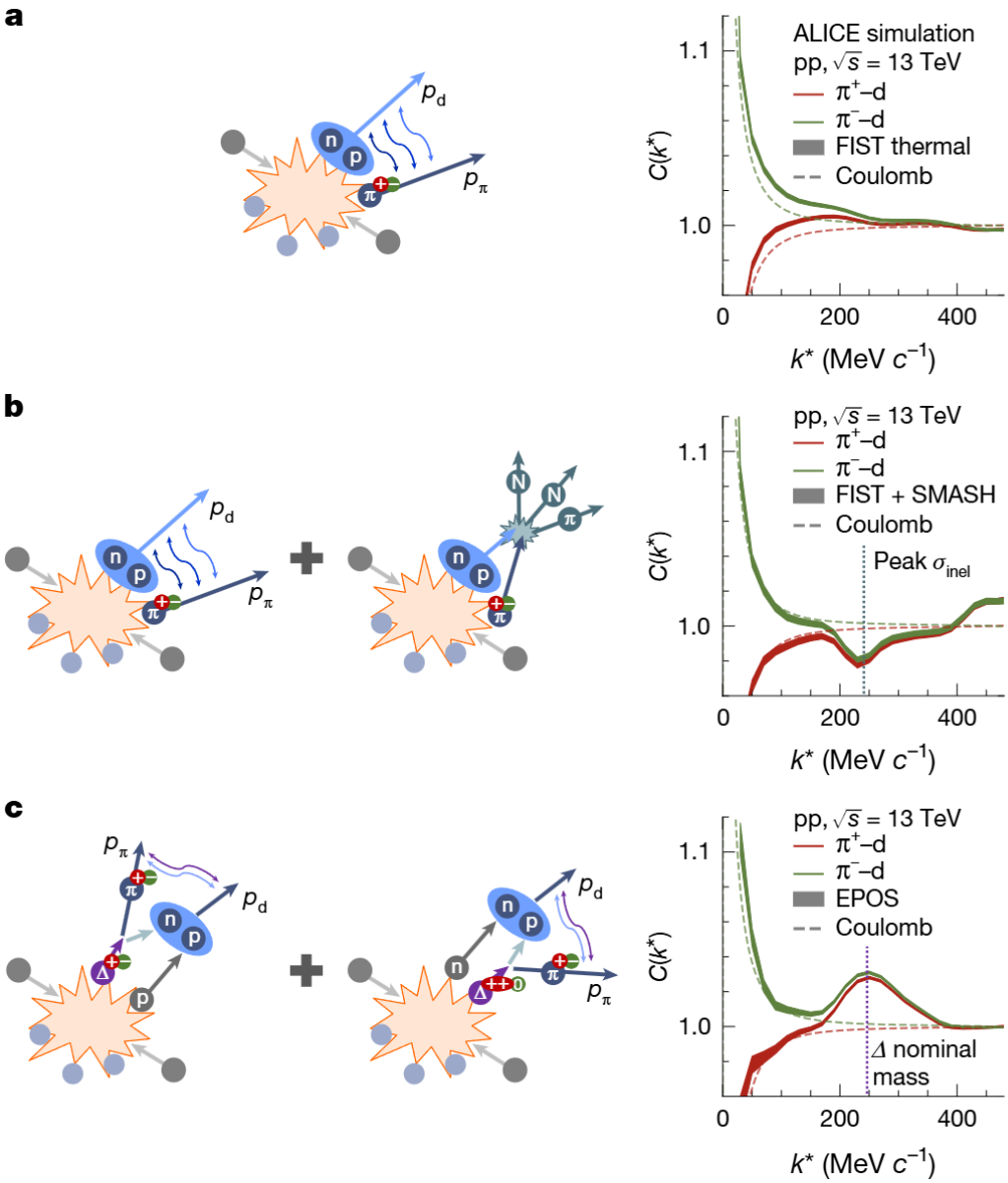

Figure 1: Schematic illustration of the two-particle correlation function in different scenarios, showing the effect of quantum statistics and of the strong interaction at low k^* [reproduced from Ref. [28]].

Unlike traditional scattering experiments, femtoscopy does not require stable targets or beams: it can probe the interaction of any pair of particles produced in high-energy collisions, including unstable and very short-lived ones, such as the Ξ^-, Ω^- hyperons or the resonances $\mathrm{D}_{s0}^*(2317)$ and $D_{s1}(2460)$. ALICE has successfully applied femtoscopy to a variety of hadron pairs in pp collisions at the LHC, e.g. p–Λ, p–Ξ^-, p–Ω^- and K^-–p [15, 16], achieving a precision comparable to that of scattering experiments and benchmarking state-of-the-art theoretical calculations, such as those of lattice QCD for the p–Ω^- interaction [17]. In the strange sector, the ALICE Collaboration has also established femtoscopic measurements with K_S^0 mesons, reporting $\mathrm{K}_\mathrm{S}^0\mathrm{K}_\mathrm{S}^0$ and $\mathrm{K}_\mathrm{S}^0\mathrm{K}^\pm$ correlation functions in pp collisions [18]. On the theory side, the femtoscopic correlation function of the DK system has been computed by Liu, Lu and Geng [19] in leading-order chiral perturbation theory with coupled channels, and a model-independent method to extract the DK interaction directly from the data has been proposed by Ikeno, Toledo and Oset [20]. These studies predict a clear suppression of the correlation function, $C(k^*) < 1$, at low k^* if $\mathrm{D}_{s0}^*(2317)$ is a DK bound state, providing a clean experimental signature to test the molecular hypothesis.

In this note, we present the first measurement of femtoscopic correlations between $\mathrm{D}^\pm$ mesons and K_S^0 mesons in pp collisions at $\sqrt{s} = 13.6$ TeV, using the data collected by ALICE during LHC Run 3. The K_S^0 is a CP eigenstate, $\mathrm{K}_\mathrm{S}^0 \approx (\mathrm{K}^0 - \overline{\mathrm{K}}^0)/\sqrt{2}$ (neglecting CP violation), so the measured $\mathrm{D}^\pm$–K_S^0 correlation function receives contributions from both the D^+K^0 ($S = +1$) and the $D^+\overline{K}^0$ ($S = -1$) interactions, whose properties are expected to differ: only the strangeness $S = +1$ channel, together with D^0K^+, is directly connected to the $\mathrm{D}_{s0}^*(2317)$ molecular picture, while the $S = -1$ channel probes a different interaction. A complete theoretical description of the $\mathrm{D}^\pm$–K_S^0 correlation function therefore requires coupled-channel calculations that account for the K^0–$\overline{\mathrm{K}}^0$ mixing. Furthermore, the correlation function is expected to exhibit peaks originating from known resonances decaying into $D^+\mathrm{K}_\mathrm{S}^0$ or $D^{*+}\mathrm{K}_\mathrm{S}^0$ pairs, in particular the $\mathrm{D}_{s2}^*(2573)^+$ and the $\mathrm{D}_{s1}(2536)^+$, whose observation provides an internal cross-check of the analysis and represents the first identification of known resonance signals in a charm–strange correlation function.

This note is organised as follows. Section 2 describes the data sample and the event selection. Sections 3 and 4 describe the reconstruction and selection of the D^+ and K_S^0 candidates, respectively. The construction of the correlation function, including the correction for the minijet background and the modeling of the source function, is discussed in Section 5. Section 6 summarises the note and gives an outlook.

2 Data sample and event reconstruction

2.1 Software package

The analysis is performed within the ALICE O2 analysis framework, which handles the online and offline processing of the Run 3 data collected in continuous-readout mode [21]. The heavy-flavour

(HF) 2- and 3-prong skimming outputs used in this analysis are organised in derived datasets produced with the AliHyperloop train system [22], and the candidate tables and pair observables are produced with the corresponding O2 analysis tasks. The final steps of the analysis are performed offline.

2.2 Analysed files and event selection

The analysis uses the minimum-bias (MB) pp collision data at $\sqrt{s} = 13.6$ TeV collected by ALICE during the 2022 and 2023 data-taking periods of LHC Run 3 [23]. The reconstruction pass used is apass7 for the LHC22 sample and apass4 for the LHC23 sample.

2.2.1 Event selection

The event selection employed is the standard `sel8` trigger condition [24], which satisfies the following criteria:

1. **TVX condition**: ensures that collisions occur close to the nominal vertex position (the expected position of the beam crossing), which helps reject beam–gas and other background vertices. The criterion is checked by verifying that the timestamps of the collision recorded by the FT0A and FT0C detectors (located along the beamline on either side of the collision point) are compatible with a collision taking place at the nominal position. Background collisions occurring away from this position would be closer to one of the two forward detectors, and would therefore be recorded earlier by that detector and later by the other one.
2. **Time-frame border cut**: close to the beginning and to the end of a time frame, the reconstruction efficiency of the candidates is lower because some of the tracks might fall into the adjacent time frame. For this reason, events close to the time-frame borders are not considered in this analysis.
3. **ITS readout-frame border cut**: this selection is applied only to real data, because the ITS readout-frame borders are not properly simulated in the Monte Carlo (MC) productions.

In addition, events with an interaction vertex outside the range $|z_{\mathrm{vtx}}| < 10$ cm are rejected. After the event selection described above, and accounting for the losses due to event merging, about 208×10^9 MB events are used in this analysis. A summary of the event selection is given in Table 1.

2.3 Experimental data

The analysis on data is operationally run in three steps. First, a linked derived dataset is produced, saving the heavy-flavour 2- and 3-prong skimming outputs with loose selections. This is mostly done

Selection criterion	Value
Trigger	`sel8`
$\lvert z_{\mathrm{vtx}} \rvert$	< 10 cm
Multiplicity	< 100

Table 1: Event selection criteria applied in this analysis.

to save CPU usage for the later analysis trains. The datasets used for the LHC22 and LHC23 periods are `HF_LHC22o_pass7_minBias_2P3PDstar` and `HF_LHC23_pass4_Thin_2P3PDstar`, respectively, produced with the AliHyperloop train system [22] (trains 701201 and 701200 for the LHC22 and LHC23 datasets, respectively). In the second step, the skimmed datasets are used to generate tables for the D^+ and K^0_S candidates. These tables are then used to pair D^+ with K^0_S and to measure the observable of interest, namely the relative momentum k^*. In the final step, the paired $\mathrm{D}^\pm$–K^0_S candidates are analysed offline to extract the genuine correlation distribution.

2.4 Monte Carlo simulations

The MC simulations used for the training of the machine-learning based selection of the D^+ candidates (Section 3) consist of the productions LHC24d3a and LHC24d3b, anchored to the 2022 data-taking conditions (reconstruction pass6). In addition, the MC samples provide the template of the D^+ signal shape used in the extraction of the pair yields (Section 5).

3 D^+ candidate reconstruction

The D^+mesons are reconstructed via their hadronic decay channel $\mathrm{D}^+ \rightarrow \pi^+\mathrm{K}^-\pi^+$ [25]. The reconstruction proceeds in three steps: a track-level preselection, the candidate building, and a further purification based on the decay topology and kinematics, described in the following.

3.1 Track preselection

The daughter tracks of the D^+candidates must satisfy a set of basic quality criteria, in order to suppress non-physical tracks produced in secondary interactions and to guarantee reliable momentum and position measurements. Table 2 lists the selection criteria applied to the π^+ and K^- candidate tracks. Besides the track quality requirements, the pseudorapidity is constrained to $|\eta| < 0.8$, since the ALICE central barrel detectors cover this acceptance range.

Track selection variable	Selection range
TPC crossed rows	> 70
Pseudorapidity $\|\eta\|$	< 0.8
Transverse momentum p_{T}	> 0.1 GeV/c
χ^2 per TPC cluster	< 4
ITS matching	at least one cluster per layer
Number of ITS clusters	> 4

Table 2: Track preselection criteria applied to the π^+ and K^- daughter tracks.

3.2 Candidate building and topological preselection

After the track selection, any pair of same-charge $\pi^+\pi^+$ tracks and one opposite-charge K^- track are combined to form a three-prong decay vertex, thus building the initial D^+candidates. Owing to the very large number of track combinations in high-energy pp collisions, this purely geometrical combination unavoidably yields a large amount of combinatorial background. A set of relatively loose hard selections is therefore applied to suppress the combinatorial background while preserving the signal efficiency. These selections exploit the decay topology, which for heavy-flavour hadrons differs significantly from that of the light-flavour background, and include:

- **Decay length**: the spatial distance between the D^+decay vertex and the primary vertex of the event. The D^+meson has an intrinsic lifetime of about 1.04 ps, corresponding to $c\tau \approx 312$ μm [25]; in the laboratory frame, the decay length is typically of the order of millimetres to centimetres owing to the Lorentz boost, producing a measurable separation between the primary and the decay vertices. Combinatorial background, in contrast, is mostly concentrated close to the primary vertex, so a lower threshold on the decay length efficiently suppresses it.

- **Daughter transverse momentum**: since the D^+mass is 1.869 GeV/c^2 [25], much larger than that of light-flavour hadrons, its decay products typically carry relatively high transverse momentum; a lower threshold on the daughter p_{T} suppresses the low-momentum combinatorial background.

- **Cosine of the pointing angle**: the cosine of the angle between the reconstructed momentum of the D^+candidate and the vector joining the primary to the decay vertex. For genuine D^+decays the momentum direction is highly aligned with the flight direction, so $\cos\theta_p$ is close to unity, while for combinatorial background it is broadly distributed.

- **Invariant-mass window**: the invariant mass of the candidate computed from the four-momenta of the decay products is required to be close to the D^+nominal mass, retaining the signal peak while rejecting most purely random combinations.

- **Particle identification (PID)**: the TPC and TOF responses of the daughter tracks are

compared with the expected ones, and the tracks are required to be compatible with the pion or kaon hypotheses within 5σ.

The preselection criteria applied in this analysis are summarised in Table 3; slightly tighter selections are used for candidates with $p_{\mathrm{T}} > 5$ GeV/c, where the topology variables are more discriminating.

Selection	$p_{\mathrm{T}} < 5$ GeV/c	$p_{\mathrm{T}} > 5$ GeV/c
Decay length	> 0.01 cm	> 0.02 cm
Daughter p_{T}	> 0.3 GeV/c	> 0.3 GeV/c
$\cos\theta_p$	> 0.85	> 0.9
Invariant-mass window	$M_{\mathrm{D^+}} \pm 0.2$ GeV/c^2	$M_{\mathrm{D^+}} \pm 0.5$ GeV/c^2
PID $\lvert n\sigma_{\mathrm{TOF}}\rvert$	< 5	< 5
PID $\lvert n\sigma_{\mathrm{TPC}}\rvert$	< 5	< 5
PID $\lvert n\sigma^{\mathrm{comb}}_{\mathrm{TPC}}\rvert$	< 5	< 5
PID $\lvert n\sigma^{\mathrm{comb}}_{\mathrm{TOF}}\rvert$	< 5	< 5

Table 3: Topological and kinematic preselection criteria applied to the $\mathrm{D^+}$candidates, for the $p_{\mathrm{T}} < 5$ GeV/c and $p_{\mathrm{T}} > 5$ GeV/c intervals.

3.3 Machine-learning based selection

The machine-learning technique used in this analysis is a multiclass boosted decision tree (BDT) classifier, implemented with the XGBoost library [26], which supports efficient multiclass training and inference. The training, hyperparameter optimisation and performance evaluation are carried out with the standardised toolchain provided by the hipe4ml software package [27].

The BDT model used in this analysis was trained in 2024 by Luca Aglietta (UniTO, INFN). The training sample includes both experimental data, from the LHC22o_pass7_small dataset, and Monte Carlo simulations, namely the LHC24d3a and LHC24d3b productions anchored to the 2022 pass6 reconstruction conditions. Since the heavy-flavour decay-topology variables (impact parameter, decay length, pointing angle, etc.) correlate strongly with the particle transverse momentum, and the signal-to-background separation differs significantly across the p_{T} range, the model is trained in independent p_{T} intervals.

The model adopts a three-class architecture: for each input $\mathrm{D^+}$candidate, it outputs three probability scores:

- **Non-prompt score**: probability that the $\mathrm{D^+}$candidate originates from the weak decay of a beauty hadron (a mixture of B^+, B^0, B_s^0 and Λ_b);
- **Prompt score**: probability that the $\mathrm{D^+}$is produced directly at the primary vertex, or from the decay of a $\mathrm{D^{*+}}$ produced at the primary vertex;

- **Background score**: probability that the candidate is a wrong combination (combinatorial background).

To purify the prompt signal and control the contamination from the different components, the BDT scores are required to satisfy the thresholds reported in Table 4.

p_{T} interval (GeV/c)	Bkg score cut (<)	Prompt score cut (>)
1–2	0.008	0.26
2–3	0.010	0.26
3–4	0.015	0.26
4–5	0.015	0.26
5–6	0.065	0.26
6–7	0.065	0.26
7–8	0.065	0.26
8–9	0.080	0.26
9–10	0.080	0.26
10–12	0.080	0.26
12–16	0.150	0.26

Table 4: BDT score thresholds applied in each p_{T} interval: upper limit on the background score and lower limit on the prompt score.

Thanks to the large data sample collected in LHC Run 3, the D^{+}sample has good statistical significance after the preselection and the BDT score selection. As an example, the invariant-mass distributions of the selected D^{+}candidates in the $1 < p_{\mathrm{T}} < 2$ GeV/c and $12 < p_{\mathrm{T}} < 16$ GeV/c intervals are shown in Figs. 2 and 3, respectively. In the analysis, D^{-}candidates are reconstructed alongside the D^{+}ones with the same procedure and selections.

3.4 Non-prompt fraction

After the machine-learning based selection described in Section 3.3, a residual contribution of non-prompt $\mathrm{D}^{\pm}$ originating from beauty-hadron decays is still present in the sample. The $\mathrm{D}^{\pm}$ produced in beauty decays are not emitted from the primary vertex and therefore do not carry the $\mathrm{D}^{\pm}$–$\mathrm{K}^{0}_{\mathrm{S}}$ interaction of interest: their contribution to the correlation function is considered to be essentially flat, i.e. free of femtoscopic structures. Nevertheless, the presence of these feed-down $\mathrm{D}^{\pm}$ dilutes the measured correlation function and suppresses the genuine signal. For this reason, an accurate estimation of the non-prompt fraction in the $\mathrm{D}^{\pm}$ sample is of crucial importance to obtain unbiased information on the $\mathrm{D}^{\pm}$–$\mathrm{K}^{0}_{\mathrm{S}}$ interaction.

The fraction of non-prompt $\mathrm{D}^{\pm}$ is estimated with a data-driven method based on the variation of the selection criteria, already adopted in previous ALICE heavy-flavour analyses [32]. The method relies on the definition of several sets of selections. For each set of selections i, the raw yield Y_i extracted from the invariant-mass fit and the acceptance-times-efficiency factors of prompt and

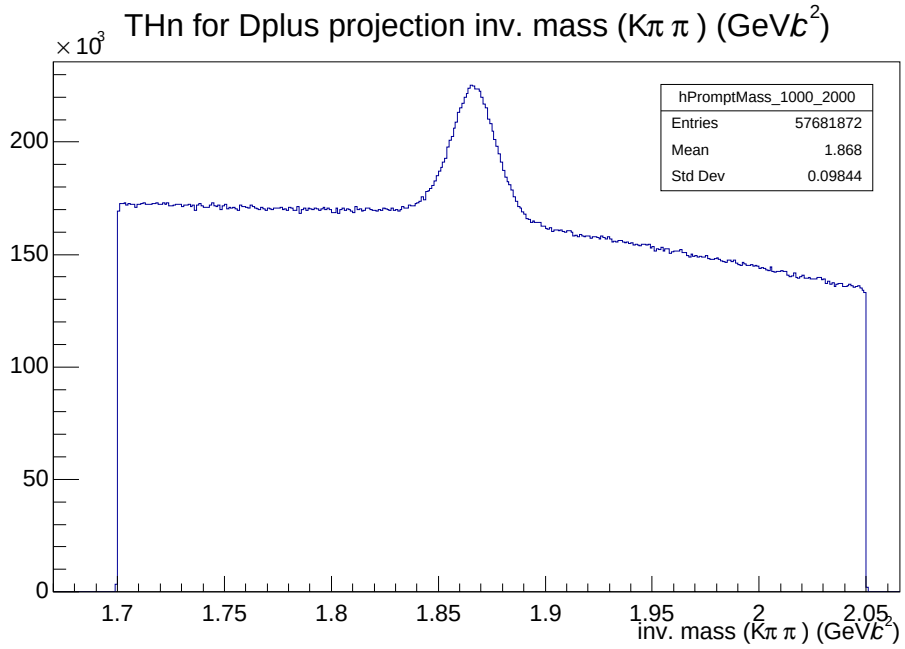

Figure 2: Invariant-mass distribution of D^+candidates in the $1 < p_{\mathrm{T}} < 2$ GeV/c interval.

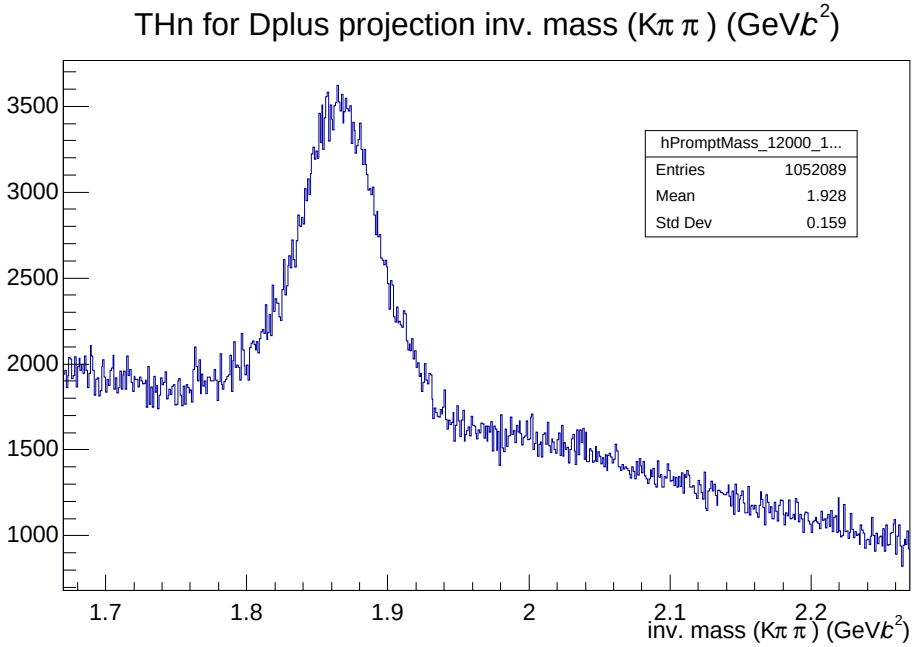

Figure 3: Invariant-mass distribution of D^+candidates in the $12 < p_{\mathrm{T}} < 16$ GeV/c interval.

non-prompt $\mathrm{D}^{\pm}$, $\varepsilon_i^{\mathrm{p}}$ and $\varepsilon_i^{\mathrm{np}}$, obtained from Monte Carlo simulations, are related to the corrected yields of prompt and non-prompt $\mathrm{D}^{\pm}$, N_{p} and N_{np}, by

$$\varepsilon_i^{\mathrm{p}}\, N_{\mathrm{p}} + \varepsilon_i^{\mathrm{np}}\, N_{\mathrm{np}} = Y_i, \tag{2}$$

for each set i. A single equation is not sufficient to determine the two unknowns N_{p} and N_{np}; therefore, n different sets of topological selections are defined, resulting in a system of n equations. For $n > 2$ the system is overdetermined, and since both the raw yields and the efficiency factors are affected by statistical and systematic uncertainties, the corrected yields are obtained through a χ^2-minimisation procedure, which provides an approximate solution of the system [32]. The prompt fraction of the sample corresponding to a given set of selections i is then defined as

$$f_i^{\mathrm{p}} = \frac{\varepsilon_i^{\mathrm{p}}\, N_{\mathrm{p}}}{\varepsilon_i^{\mathrm{p}}\, N_{\mathrm{p}} + \varepsilon_i^{\mathrm{np}}\, N_{\mathrm{np}}}, \tag{3}$$

and the non-prompt fraction is simply $f_i^{\mathrm{np}} = 1 - f_i^{\mathrm{p}}$.

In this analysis, the different cut sets are defined by varying the selection on the non-prompt output score of the machine-learning classifier only, while the selections on the combinatorial-background and prompt scores are kept fixed (Table 4), in order to reduce the large combinatorial background contribution and to extend the coverage of the prompt fraction. For each p_{T} interval, the loosest and tightest selections on the non-prompt score define the scan over the cut sets, which is performed in 22 steps between the two extreme selections. The loosest and tightest selections used for each p_{T} interval are summarised in Table 5.

p_{T} interval (GeV/c)	Loosest FD-score cut	Tightest FD-score cut
1–2	0.170	0.962
2–3	0.130	0.900
3–4	0.120	0.802
4–5	0.120	0.758
5–6	0.090	0.706
6–7	0.060	0.698
7–8	0.060	0.698
8–10	0.080	0.696
10–12	0.080	0.696
12–16	0.050	0.710

Table 5: Range of the selection on the non-prompt (FD) output score of the machine-learning classifier defining the scan over the cut sets, for each p_{T} interval. The non-prompt score takes values in $[0, 1]$.

The minimisation is then repeated for each cut set, and the resulting prompt and non-prompt fractions as a function of the cut set are used to extract the central value of the non-prompt fraction and its uncertainty. The results of the minimisation procedure for each p_{T} interval are

shown in Figs. 4–13. Finally, the prompt and non-prompt fractions corresponding to the selections adopted in this analysis are extracted from the minimisation; the resulting fractions as a function of p_{T} are shown in Fig. 14.

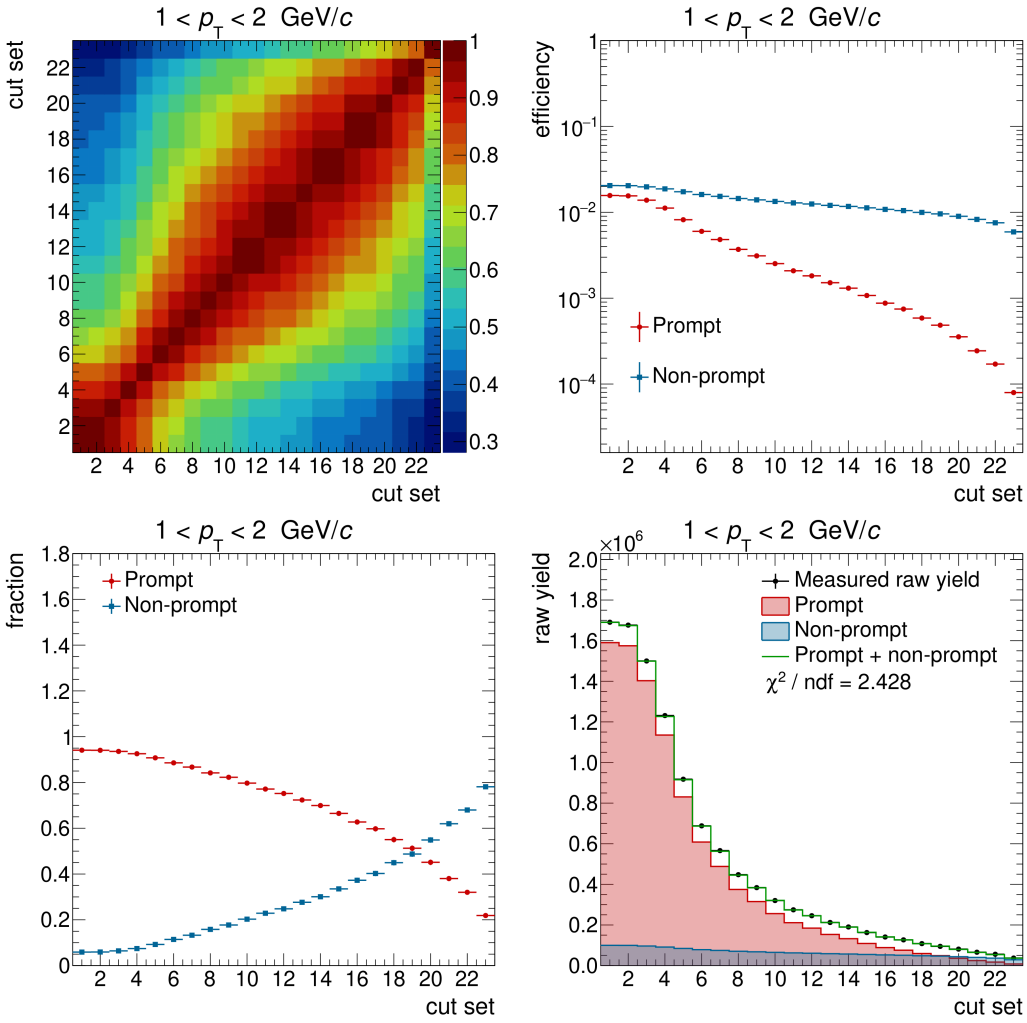

Figure 4: The correlation matrix (top-left), the acceptance-times-efficiency factors for prompt and non-prompt $\mathrm{D}^{\pm}$ (top-right), the resulting prompt and non-prompt fractions (bottom-left), and the raw yield with the prompt and non-prompt contributions obtained from the minimisation procedure (bottom-right), shown for the interval $1 < p_{\mathrm{T}} < 2$ GeV/c.

4 K^0_S selection

4.1 Properties of the K^0_S meson

In the femtoscopic correlation measurement of the DK system, the neutral kaon is probed through its short-lived component, the $\mathrm{K}^0_{\mathrm{S}}$. The K^0 meson is composed of a down quark and an anti-strange

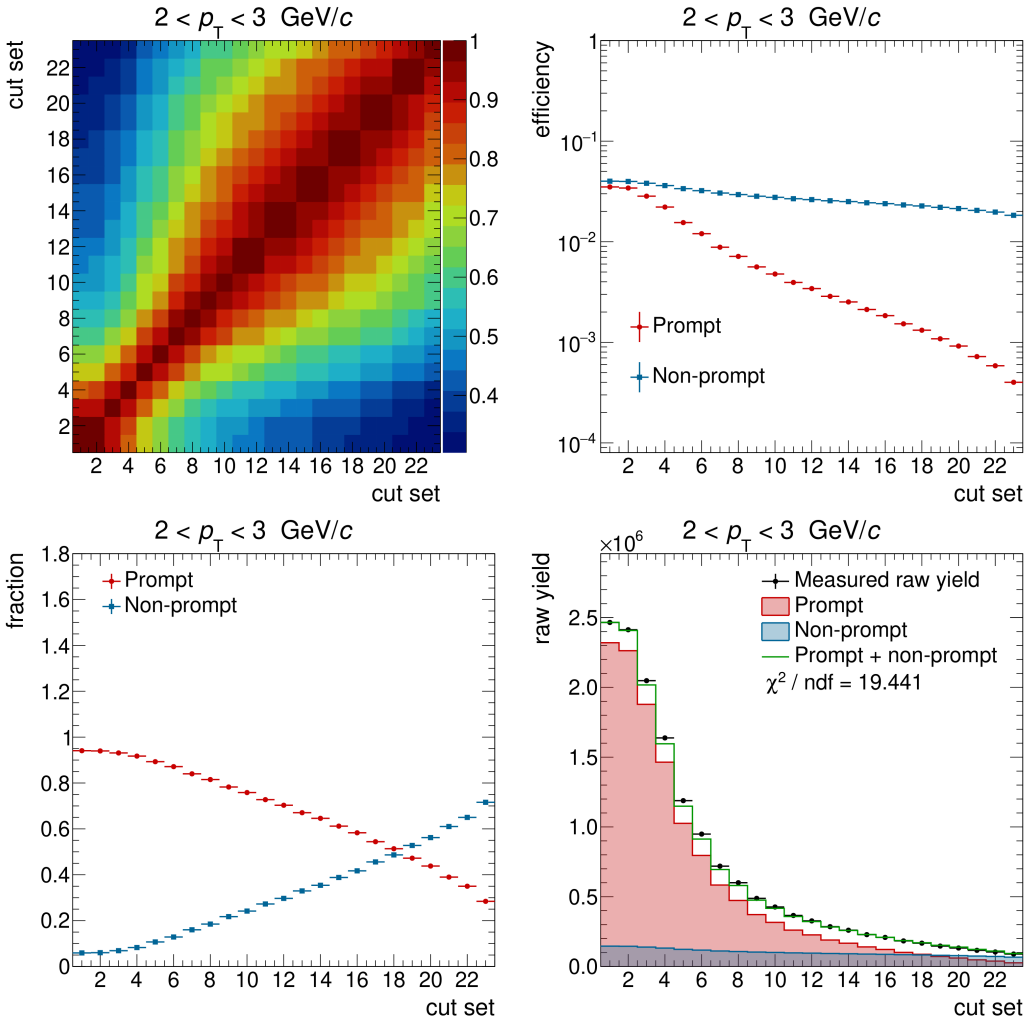

Figure 5: The correlation matrix (top-left), the acceptance-times-efficiency factors for prompt and non-prompt $D^{\pm}$ (top-right), the resulting prompt and non-prompt fractions (bottom-left), and the raw yield with the prompt and non-prompt contributions obtained from the minimisation procedure (bottom-right), shown for the interval $2 < p_T < 3$ GeV/c.

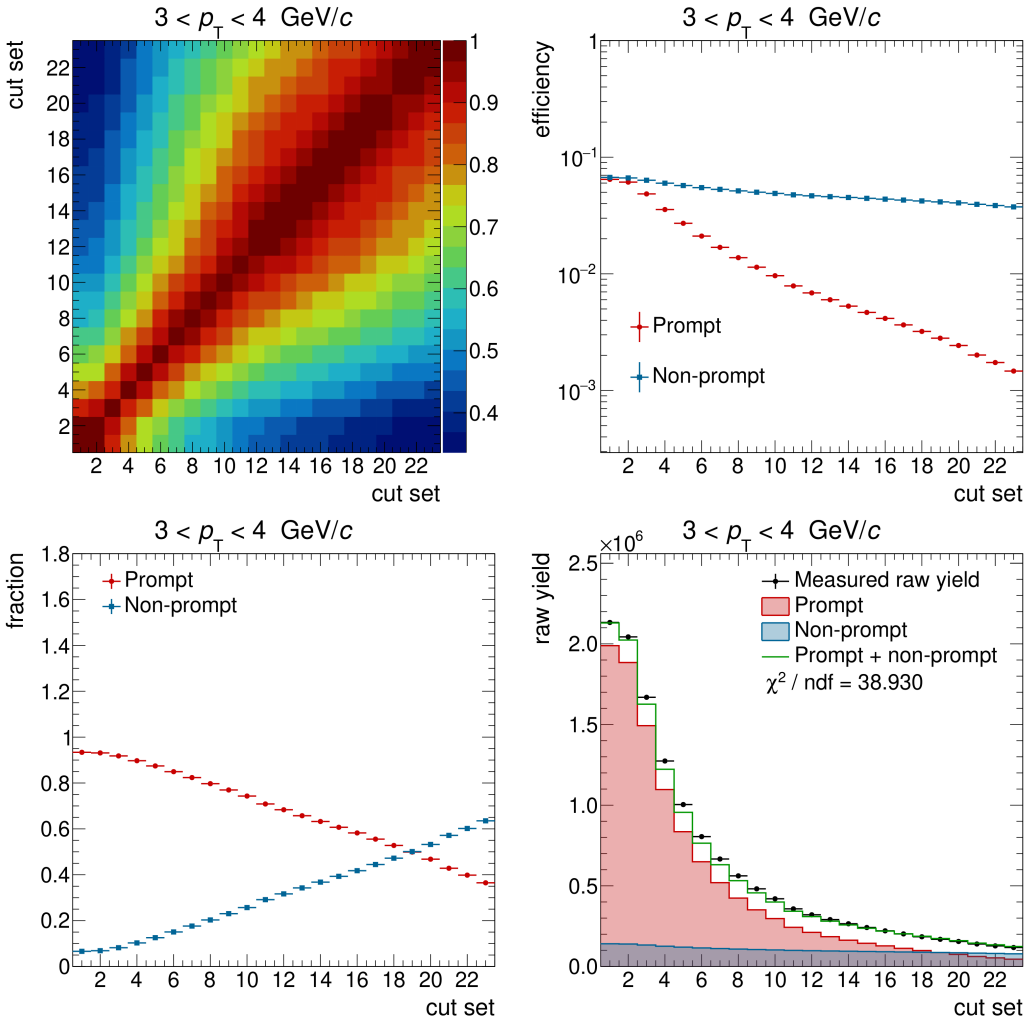

Figure 6: The correlation matrix (top-left), the acceptance-times-efficiency factors for prompt and non-prompt $D^{\pm}$ (top-right), the resulting prompt and non-prompt fractions (bottom-left), and the raw yield with the prompt and non-prompt contributions obtained from the minimisation procedure (bottom-right), shown for the interval $3 < p_T < 4$ GeV/c.

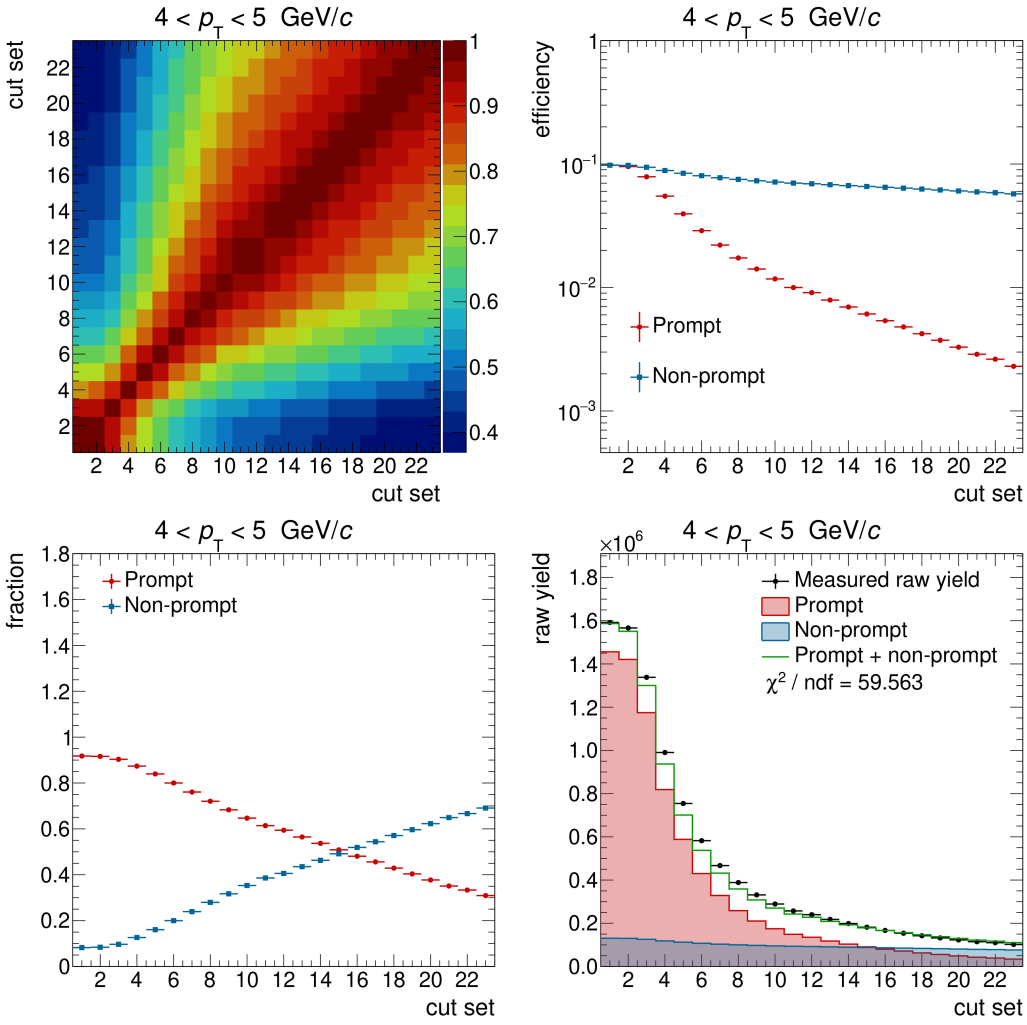

Figure 7: The correlation matrix (top-left), the acceptance-times-efficiency factors for prompt and non-prompt $D^{\pm}$ (top-right), the resulting prompt and non-prompt fractions (bottom-left), and the raw yield with the prompt and non-prompt contributions obtained from the minimisation procedure (bottom-right), shown for the interval $4 < p_T < 5$ GeV/c.

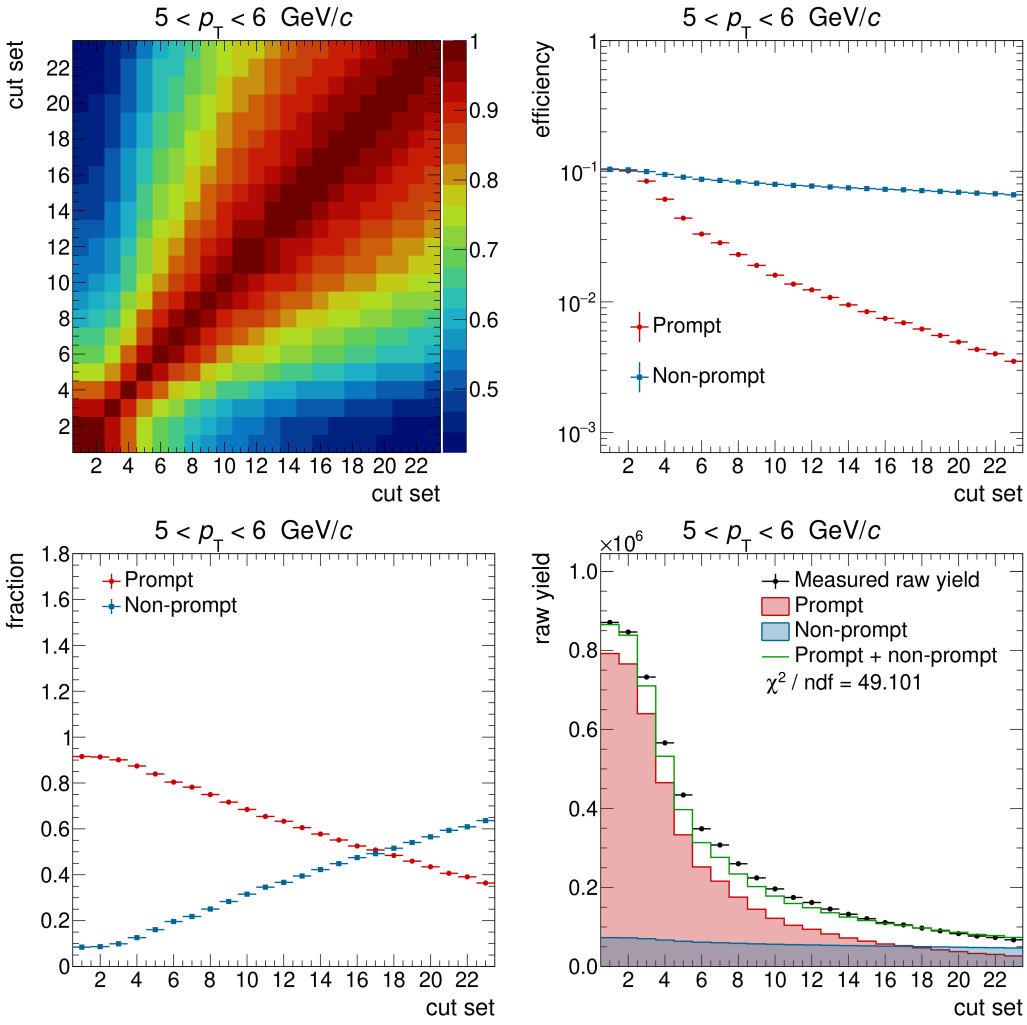

Figure 8: The correlation matrix (top-left), the acceptance-times-efficiency factors for prompt and non-prompt $D^{\pm}$ (top-right), the resulting prompt and non-prompt fractions (bottom-left), and the raw yield with the prompt and non-prompt contributions obtained from the minimisation procedure (bottom-right), shown for the interval $5 < p_T < 6$ GeV/c.

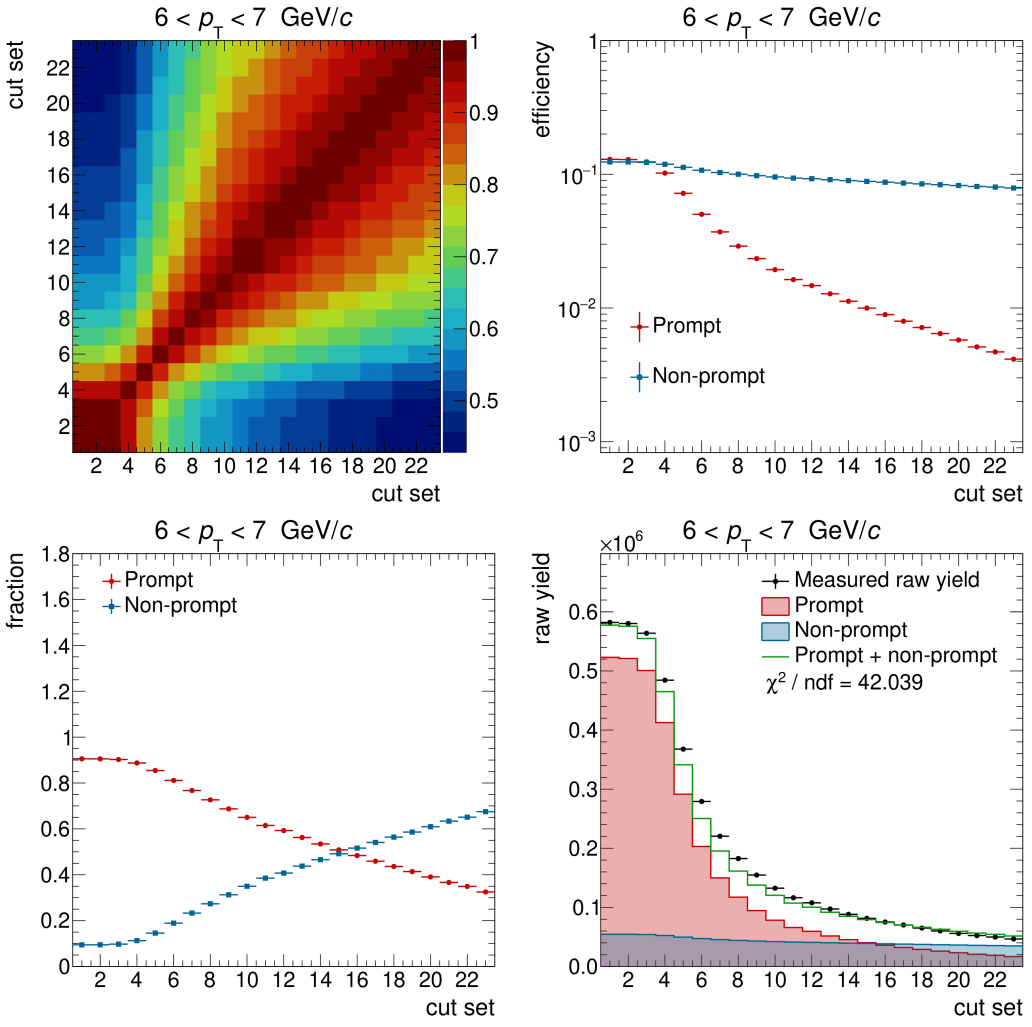

Figure 9: The correlation matrix (top-left), the acceptance-times-efficiency factors for prompt and non-prompt $D^{\pm}$ (top-right), the resulting prompt and non-prompt fractions (bottom-left), and the raw yield with the prompt and non-prompt contributions obtained from the minimisation procedure (bottom-right), shown for the interval $6 < p_T < 7$ GeV/c.

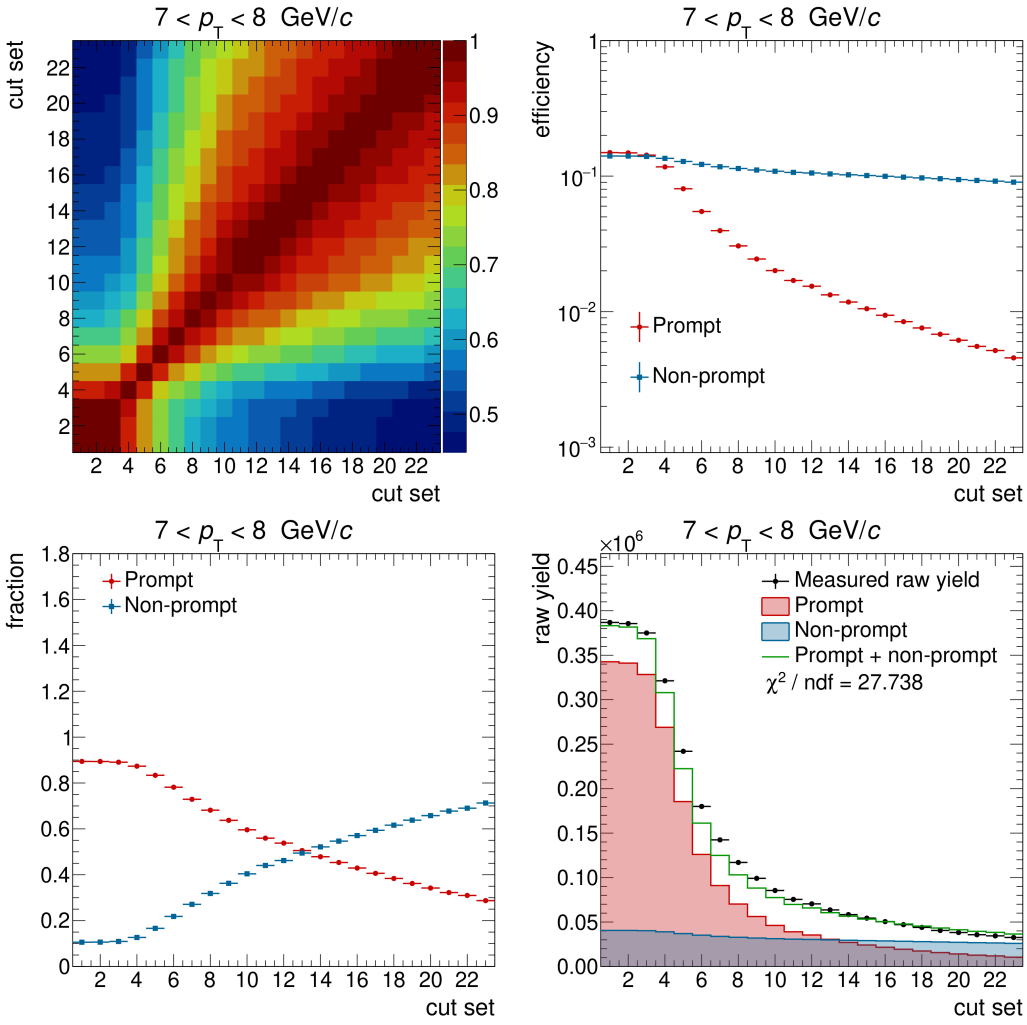

Figure 10: The correlation matrix (top-left), the acceptance-times-efficiency factors for prompt and non-prompt $D^{\pm}$ (top-right), the resulting prompt and non-prompt fractions (bottom-left), and the raw yield with the prompt and non-prompt contributions obtained from the minimisation procedure (bottom-right), shown for the interval $7 < p_T < 8$ GeV/c.

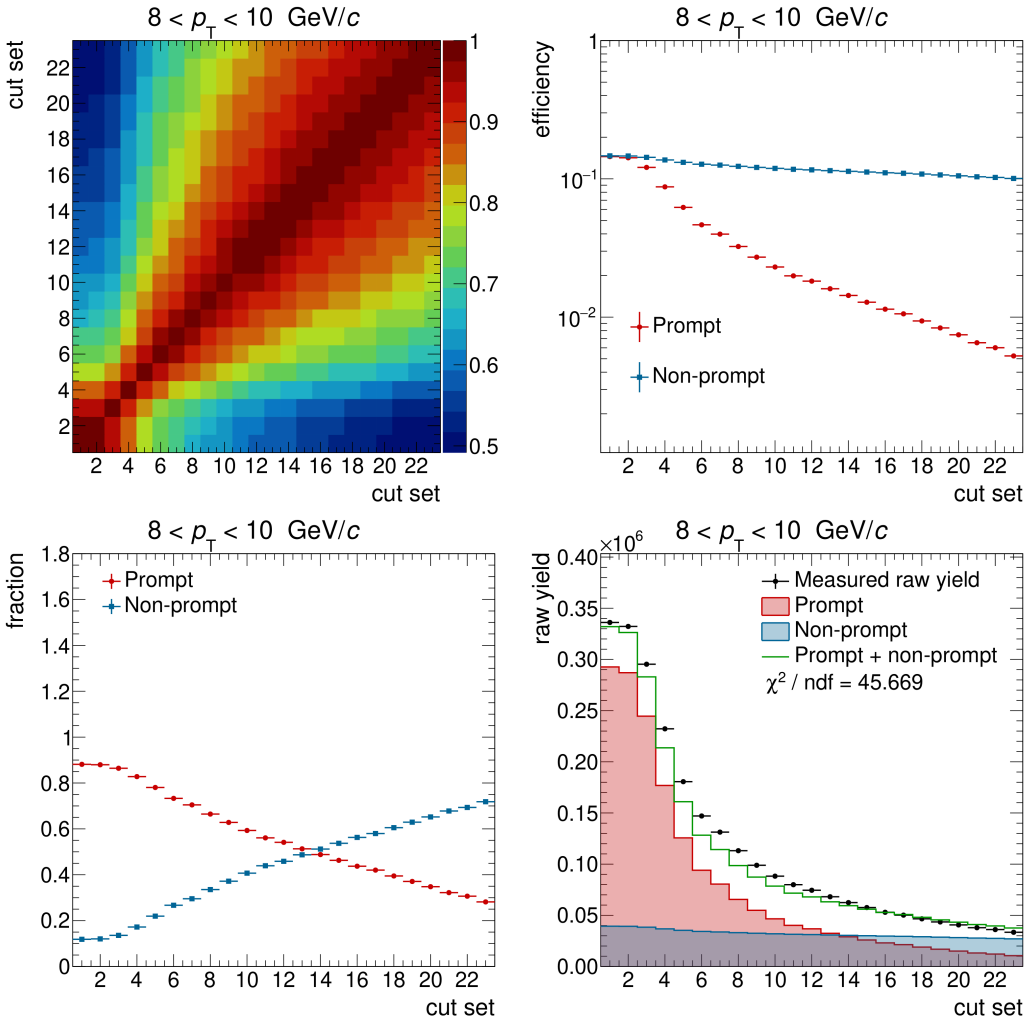

Figure 11: The correlation matrix (top-left), the acceptance-times-efficiency factors for prompt and non-prompt $D^{\pm}$ (top-right), the resulting prompt and non-prompt fractions (bottom-left), and the raw yield with the prompt and non-prompt contributions obtained from the minimisation procedure (bottom-right), shown for the interval $8 < p_T < 10$ GeV/c.

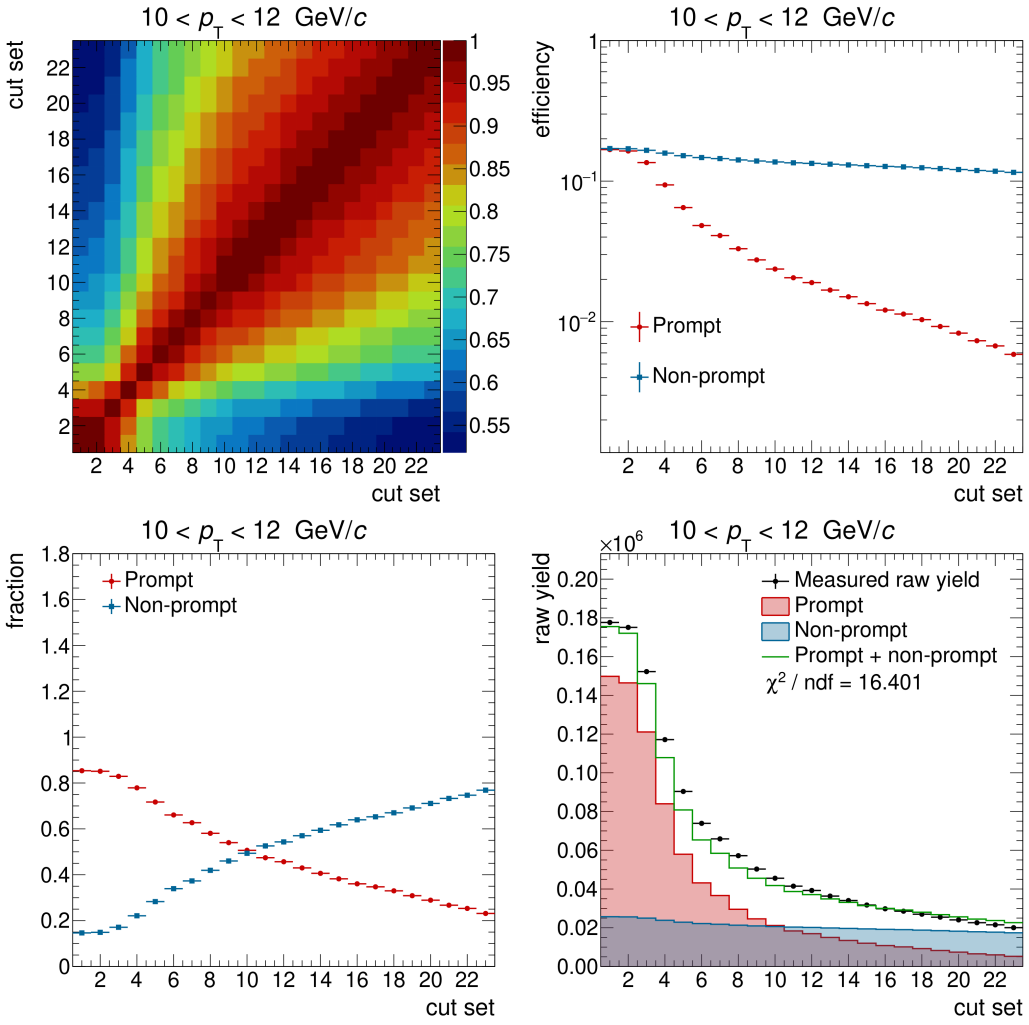

Figure 12: The correlation matrix (top-left), the acceptance-times-efficiency factors for prompt and non-prompt $D^{\pm}$ (top-right), the resulting prompt and non-prompt fractions (bottom-left), and the raw yield with the prompt and non-prompt contributions obtained from the minimisation procedure (bottom-right), shown for the interval $10 < p_T < 12$ GeV/c.

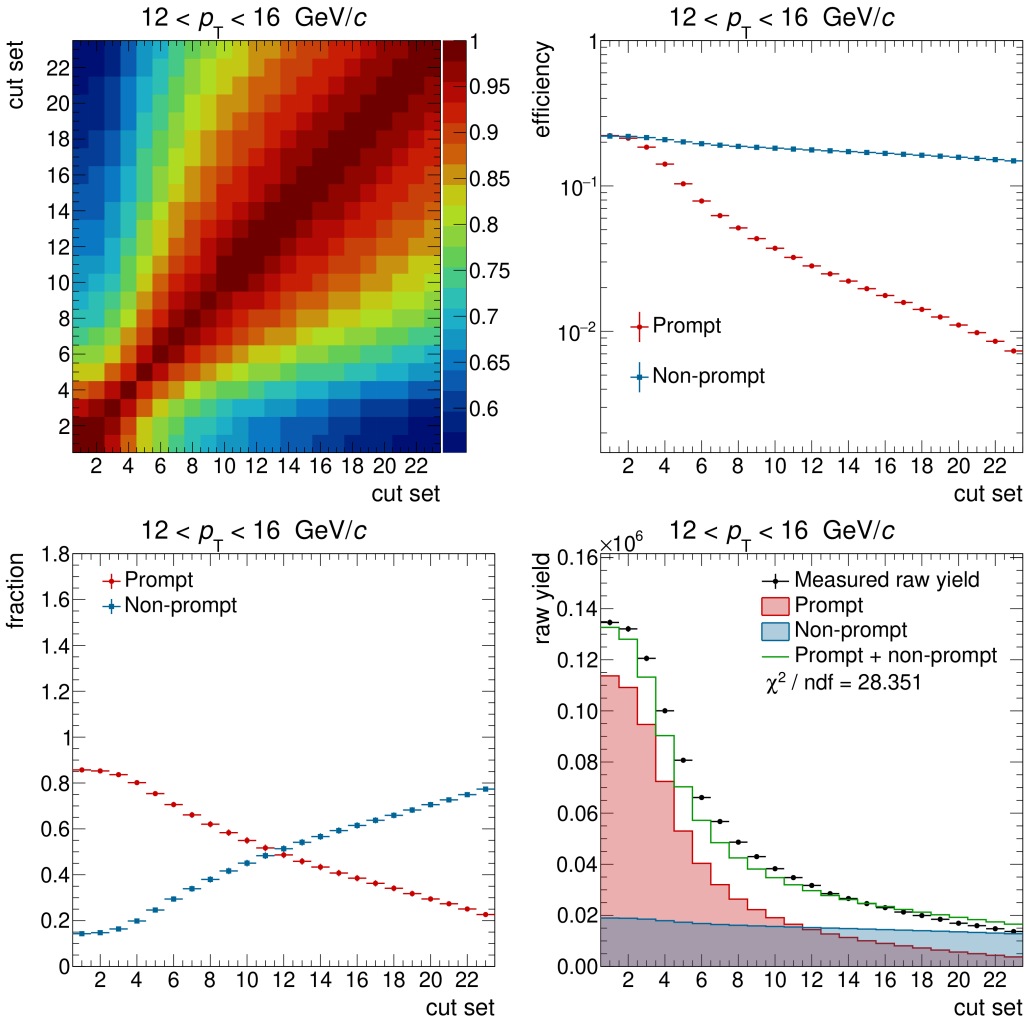

Figure 13: The correlation matrix (top-left), the acceptance-times-efficiency factors for prompt and non-prompt $D^{\pm}$ (top-right), the resulting prompt and non-prompt fractions (bottom-left), and the raw yield with the prompt and non-prompt contributions obtained from the minimisation procedure (bottom-right), shown for the interval $12 < p_T < 16$ GeV/c.

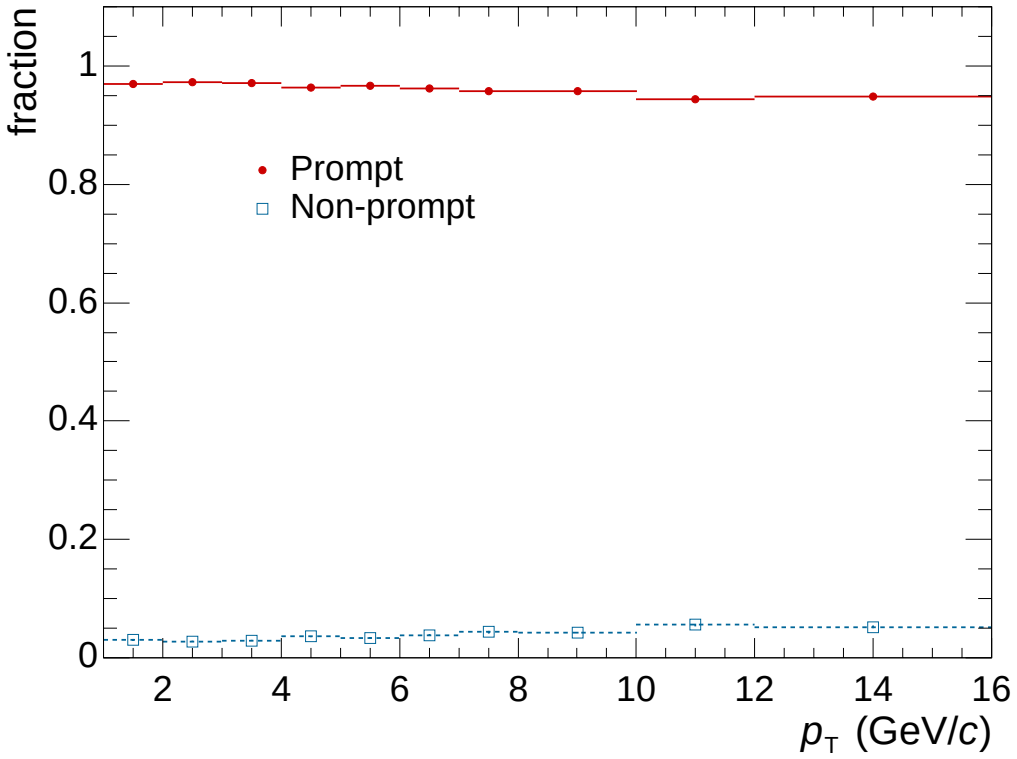

Figure 14: Final prompt and non-prompt fractions of the $\mathrm{D}^{\pm}$ candidates as a function of p_{T}, evaluated with the selections adopted in this analysis.

quark ($d\bar{s}$, strangeness $S = +1$), while its antiparticle $\overline{\mathrm{K}}^0$ is composed of an anti-down quark and a strange quark ($\bar{d}s$, $S = -1$). In strong interactions, K^0 and $\overline{\mathrm{K}}^0$ are eigenstates with definite strangeness. However, kaons can decay through the weak interaction, under which K^0 and $\overline{\mathrm{K}}^0$ are no longer eigenstates: their linear combinations form the two mass eigenstates K^0_S and K^0_L [25]. Because of this mixing mechanism, a K^0 or a $\overline{\mathrm{K}}^0$ produced in a collision immediately enters the oscillation process and propagates as a superposition of K^0_S and K^0_L, which makes the direct detection of the flavour eigenstates impossible and justifies the use of the K^0_S as the experimental probe of the neutral kaon.

The K^0_S is reconstructed via the decay channel $\mathrm{K}^0_\mathrm{S} \to \pi^+\pi^-$, which has a branching ratio of about 69.2% and a mean proper decay length of $c\tau \approx 2.7$ cm [25]. In the ALICE central barrel, this decay appears as the characteristic V0 topology: two charged tracks intersecting at a secondary vertex displaced from the primary vertex. This topology allows the K^0_S to be efficiently separated from the combinatorial background. In contrast, the K^0_L is neutral, has a decay length of tens of metres, and can only be detected indirectly, with much lower reconstruction efficiency and precision. Based on these physics and experimental considerations, the K^0_S is selected as the neutral-kaon probe in this analysis.

4.2 Candidate reconstruction and selection

Similarly to the D^+ case, the K^0_S candidates are built by combining two opposite-charge tracks that form a two-prong (V0) decay vertex. The applied selection criteria concern the track quality as well as the decay topology and kinematics, and are summarised in Table 6:

- **Track TPC clusters**: the number of TPC clusters of the daughter tracks is required to be large enough to guarantee a good reconstruction quality;
- **Daughter DCA**: the distance of closest approach (DCA) of the daughter tracks to the primary vertex. Since the K^0_S decay length is about 2.7 cm, its daughter tracks exhibit a significantly non-zero DCA: a lower threshold rejects particles produced directly at the primary vertex, while an upper threshold removes daughters originating from higher-order decays;
- **Pseudorapidity**: $|\eta| < 0.8$ for the daughter tracks, within the ALICE central-barrel acceptance;
- **Transverse momentum**: $0.3 < p_\mathrm{T} < 10$ GeV/c for the daughter tracks;
- **Cosine of the pointing angle**: since the K^0_S is neutral, its momentum direction is highly aligned with its flight direction; requiring $\cos\theta_p > 0.99$ ensures that the kinematic direction of the candidate is consistent with its geometrical displacement, which is one of the key topological criteria to identify genuine V0 decays;

- **Invariant-mass window**: under the $\pi^+\pi^-$ mass hypothesis, the invariant mass of the candidate is required to lie in the window $0.45 < M < 0.55$ GeV/c^2, rejecting the combinatorial background far from the signal peak;
- **Particle identification**: the daughters are required to be compatible with the pion hypothesis within $|n\sigma^{\pi}_{\mathrm{comb}}| < 5$, using the combined TPC–TOF information.

Selection variable	Selection
Track TPC clusters	> 80
Daughter DCA	$0.05 < \mathrm{DCA} < 1.2$ cm
Daughter $\lvert\eta\rvert$	< 0.8
p_{T}	$0.3 < p_{\mathrm{T}} < 10$ GeV/c
$\cos\theta_p$	> 0.99
Invariant-mass window	$0.45 < M < 0.55$ GeV/c^2
PID $\lvert n\sigma^{\pi}_{\mathrm{comb}}\rvert$	< 5

Table 6: Selection criteria applied to the $\mathrm{K}^0_{\mathrm{S}}$ candidates and their daughter tracks.

Thanks to the well-established $\mathrm{K}^0_{\mathrm{S}}$ reconstruction and selection procedure, the $\mathrm{K}^0_{\mathrm{S}}$ signal is highly significant after the selections described above, as can be seen from the invariant-mass distribution shown in Fig. 15 (the nominal $\mathrm{K}^0_{\mathrm{S}}$ mass is 0.497 GeV/c^2 [25]). Given the high signal significance, all $\mathrm{K}^0_{\mathrm{S}}$ candidates are treated as genuine particles in the subsequent correlation analysis.

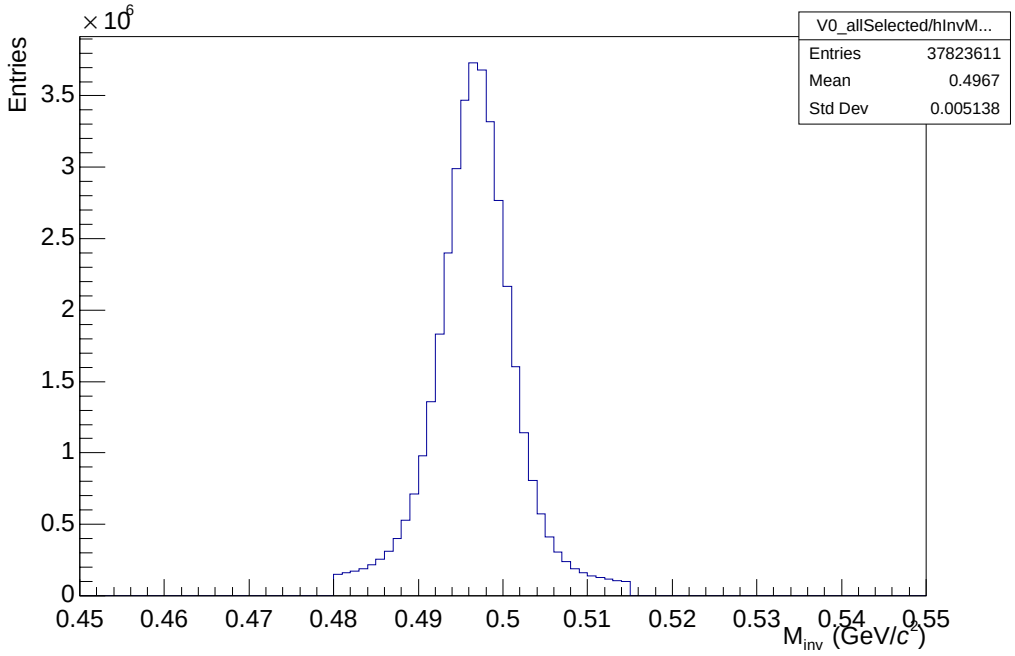

Figure 15: Invariant-mass distribution of the $\mathrm{K}^0_{\mathrm{S}}$ candidates, reconstructed via the $\mathrm{K}^0_{\mathrm{S}} \to \pi^+\pi^-$ decay channel.

5 The correlation function

5.1 Definition of the correlation function

The theoretical definition of the correlation function given in Section 1, Eq. (1), is connected to the experimental observables by rewriting it as [29]

$$C(k^*) = N \frac{A(k^*)}{B(k^*)}, \tag{4}$$

where $k^* = |\vec{p}_1^{\,*} - \vec{p}_2^{\,*}|/2$ is the relative momentum of the pair in its rest frame, $\vec{p}_1^{\,*}$ and $\vec{p}_2^{\,*}$ being the momenta of the two particles in that frame. $A(k^*)$ is the distribution of k^* for all same-event pairs, i.e. D^+ candidates paired only with K^0_S candidates belonging to the same event. $B(k^*)$ is the reference distribution of uncorrelated pairs, obtained experimentally with the event-mixing technique [30]. N is a normalisation factor: since $C(k^*)$ is expected to approach unity at high k^*, where the pairs are uncorrelated, N is tuned so that the measured correlation function is normalised to unity in the high-k^* region. In this analysis, the normalisation is performed by requiring the mean of $C(k^*)$ in the interval $1 < k^* < 2$ GeV/c to be unity.

5.2 Event-mixing technique

To avoid biases and acceptance effects of the detector system, D^+ and K^0_S candidates from different events are only paired when the corresponding events have similar z-vertex position and multiplicity. In this analysis, the z-vertex is binned in steps of 2.5 cm over the range $[-10, 10]$ cm, and the multiplicity in steps of 25 over the range $[0, 100]$. The mixing is performed by iterating over the events of each bin and pairing the D^+ candidates of the current event with the K^0_S candidates of the events stored in a buffer; a buffer size of 50 is used in this analysis.

5.3 Extraction of the pair yields

The k^* distribution of the mixed pairs is not pure, since it contains fake D^+ candidates originating from wrong combinations. Therefore, for each k^* interval, the genuine D^+ yield is extracted from an invariant-mass fit of the D^+ candidates in the pair, integrating the signal within $\pm 3\sigma$ around the peak.

The k^* range is divided into three intervals, $0 < k^* < 0.48$, $0.48 < k^* < 1.28$ and $1.28 < k^* < 2.0$ GeV/c, with a non-uniform binning inside: a bin width of 0.02 GeV/c is used in the region $0.12 < k^* < 0.44$ GeV/c and 0.04 GeV/c elsewhere. This choice is motivated by the two resonances visible in the correlation function: the peaks of $\mathrm{D}^*_{s2}(2573)^+$ and $\mathrm{D}_{s1}(2536)^+$ are located at $k^* \approx 0.42$ and 0.15 GeV/c, respectively, and the finer binning in the 0.12–0.44 GeV/c region allows the width of the two resonance peaks to be resolved and compared with the known values.

The two resonances indeed differ strongly in their natural widths: $\Gamma(\mathrm{D}_{s1}(2536)^+) = 0.92$ MeV and $\Gamma(\mathrm{D}^*_{s2}(2573)^+) = 16.9$ MeV [25], i.e. almost a factor of 20. This difference reflects the decay dynamics: $\mathrm{D}_{s1}(2536)^+$ decays to D^*K only about 27 MeV above the D^*K threshold, so the available phase space is very limited, and the D-wave centrifugal barrier ($\Gamma \propto p^{2L+1} = p^5$, p being the decay momentum) suppresses its decay further, making the resonance very narrow. In contrast, $\mathrm{D}^*_{s2}(2573)^+$ decays to DK with about 200 MeV of phase space, and its width is correspondingly much larger. In the $\mathrm{D}^\pm$–K^0_S correlation function, $\mathrm{D}^*_{s2}(2573)^+ \to D^+\mathrm{K}^0_\mathrm{S}$ contributes directly with its Breit–Wigner width, while $\mathrm{D}_{s1}(2536)^+ \to D^{*+}\mathrm{K}^0_\mathrm{S}$, followed by $D^{*+} \to D^+\pi^0$, appears as a feed-down peak that remains narrow, since the unobserved π^0 carries little momentum.

The D^+ invariant-mass distribution is described by a double Crystal Ball (DCB) function [31] for the signal and by a second-order Chebyshev polynomial for the combinatorial background. The DCB function consists of a Gaussian core smoothly joined to power-law tails on both sides, which properly describe the asymmetric tails of the signal shape. For the mixed-event pairs, the tail parameters of the DCB are fixed to the values extracted from the D^+ Monte Carlo sample, which, being background-free, describes the tails more accurately than the data, while the peak position and width are left free in the fit. For the same-event pairs, the available statistics is significantly lower; all parameters are therefore fixed to the values obtained from the corresponding k^* interval of the mixed-event fits, which reduces the impact of statistical fluctuations. Examples of the invariant-mass fits for the mixed-event and same-event pairs in the three k^* intervals are shown in Figs. 16–18 and Figs. 19–21, respectively.

5.4 Raw correlation function

After extracting the k^* distributions of the same-event and mixed-event pairs in each interval, the raw correlation functions are computed according to Eq. (4). The D^+–K^0_S and D^-–K^0_S correlation functions are found to be consistent with each other within the uncertainties; the two charge combinations are therefore merged, and the analysis proceeds with the combined $\mathrm{D}^\pm$–K^0_S pairs. The selected $\mathrm{D}^\pm$ candidates have an average prompt score above 0.96; the extracted raw yields are therefore dominated by prompt $\mathrm{D}^\pm$. Figure 22 shows the raw k^* distributions of the merged $\mathrm{D}^\pm$–K^0_S pairs for the same-event (SE) and mixed-event (ME) samples, and Fig. 23 shows the corresponding normalised yields, where the normalisation constant N is obtained by requiring the mean of the yield ratio in the interval $1 < k^* < 2$ GeV/c to be unity. The resulting raw correlation function is shown in Fig. 24.

Two prominent peaks are visible in the raw correlation function, originating from the decays of known resonances into $D^{*+}\mathrm{K}^0_\mathrm{S}$ and $D^+\mathrm{K}^0_\mathrm{S}$ pairs, respectively. The peak at $M = 2.569$ GeV/c^2 is associated with the $\mathrm{D}^*_{s2}(2573)^+$ meson, which decays directly into $D^+\mathrm{K}^0_\mathrm{S}$: this value agrees with the PDG mass of 2569.1 MeV/c^2 [25]. The peak at $M = 2.400$ GeV/c^2 is associated with the $\mathrm{D}_{s1}(2536)^+$ meson, which decays into $D^{*+}\mathrm{K}^0_\mathrm{S}$, the D^{*+} subsequently decaying into $D^+\pi^0$; since the π^0 is not reconstructed, the position of this peak corresponds to the mass difference

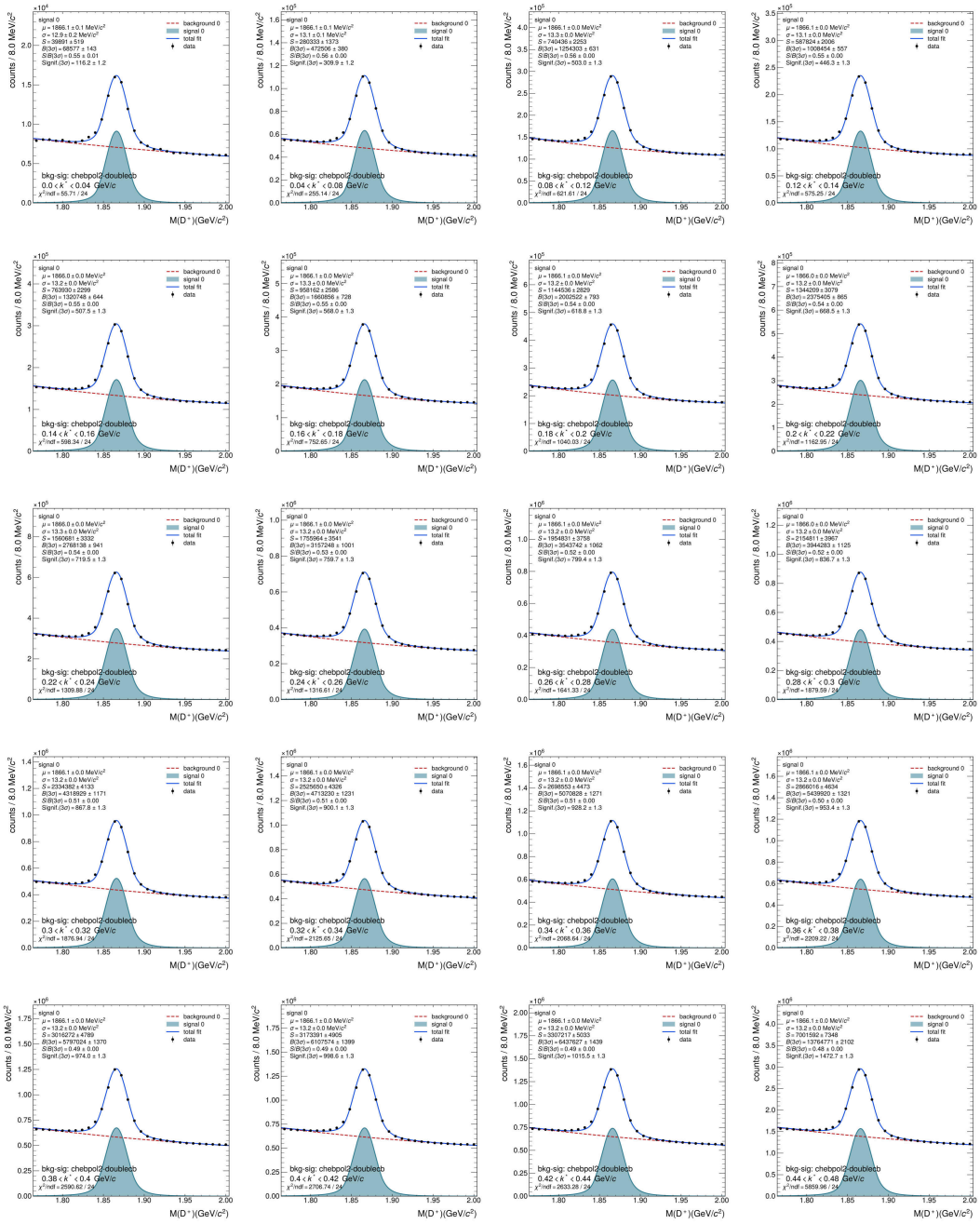

Figure 16: Invariant-mass distribution of D^+ candidates in mixed-event pairs in the $0 < k^* < 0.48$ GeV/c interval, with the result of the fit (blue line: total, red dashed line: background, cyan line: signal).

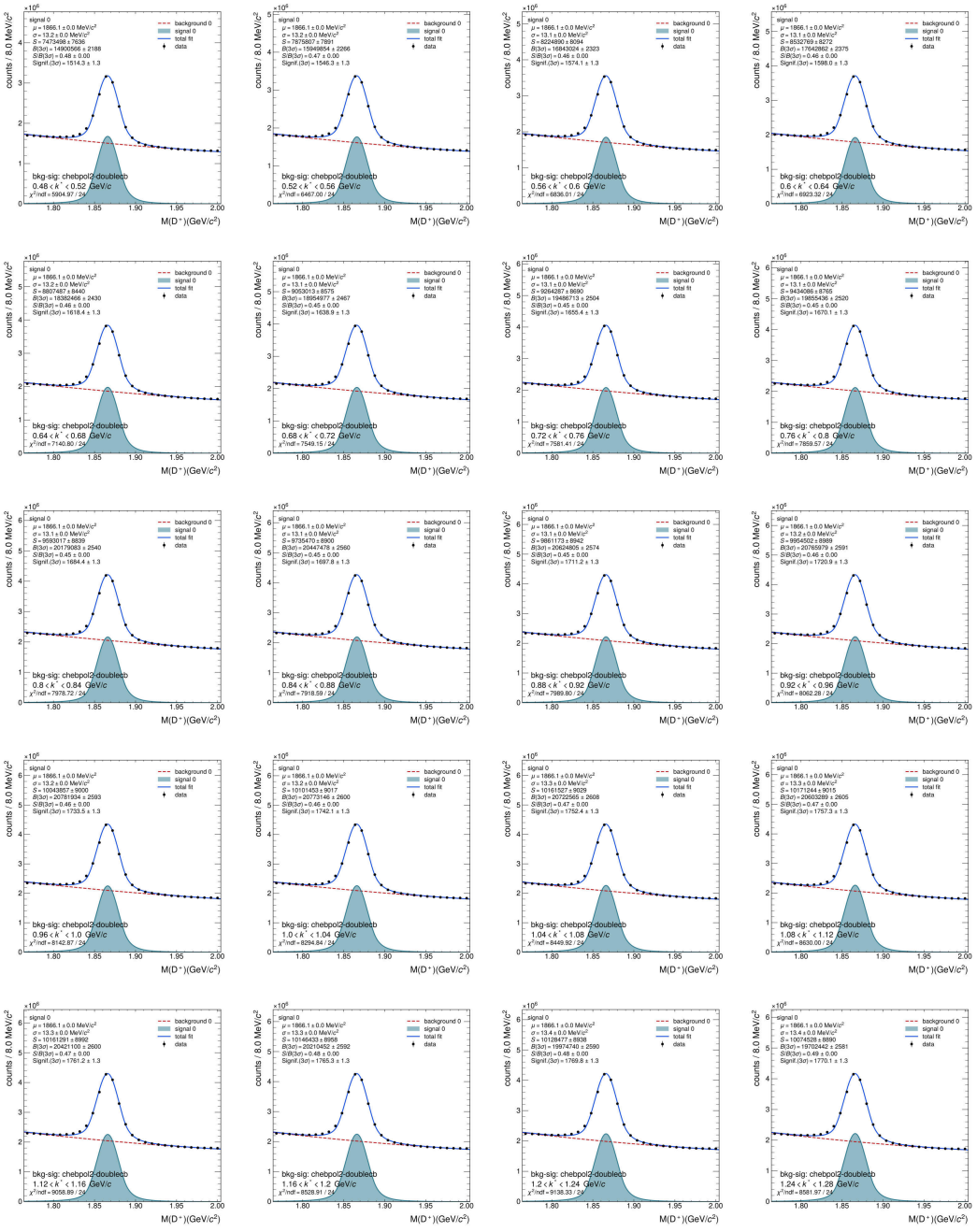

Figure 17: Invariant-mass distribution of D^+ candidates in mixed-event pairs in the $0.48 < k^* < 1.28$ GeV/c interval, with the result of the fit (blue line: total, red dashed line: background, cyan line: signal).

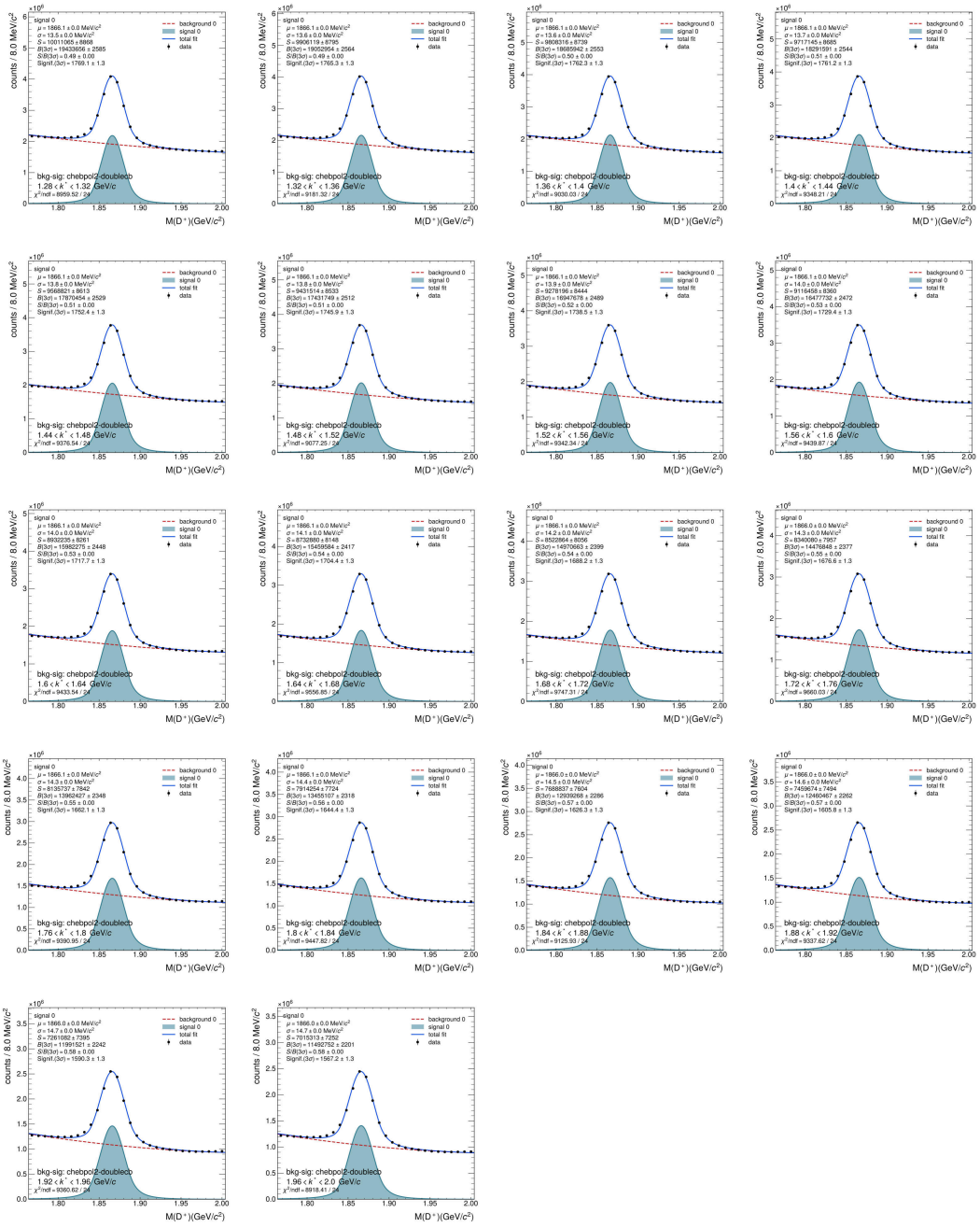

Figure 18: Invariant-mass distribution of D^+ candidates in mixed-event pairs in the $1.28 < k^* < 2.0$ GeV/c interval, with the result of the fit (blue line: total, red dashed line: background, cyan line: signal).

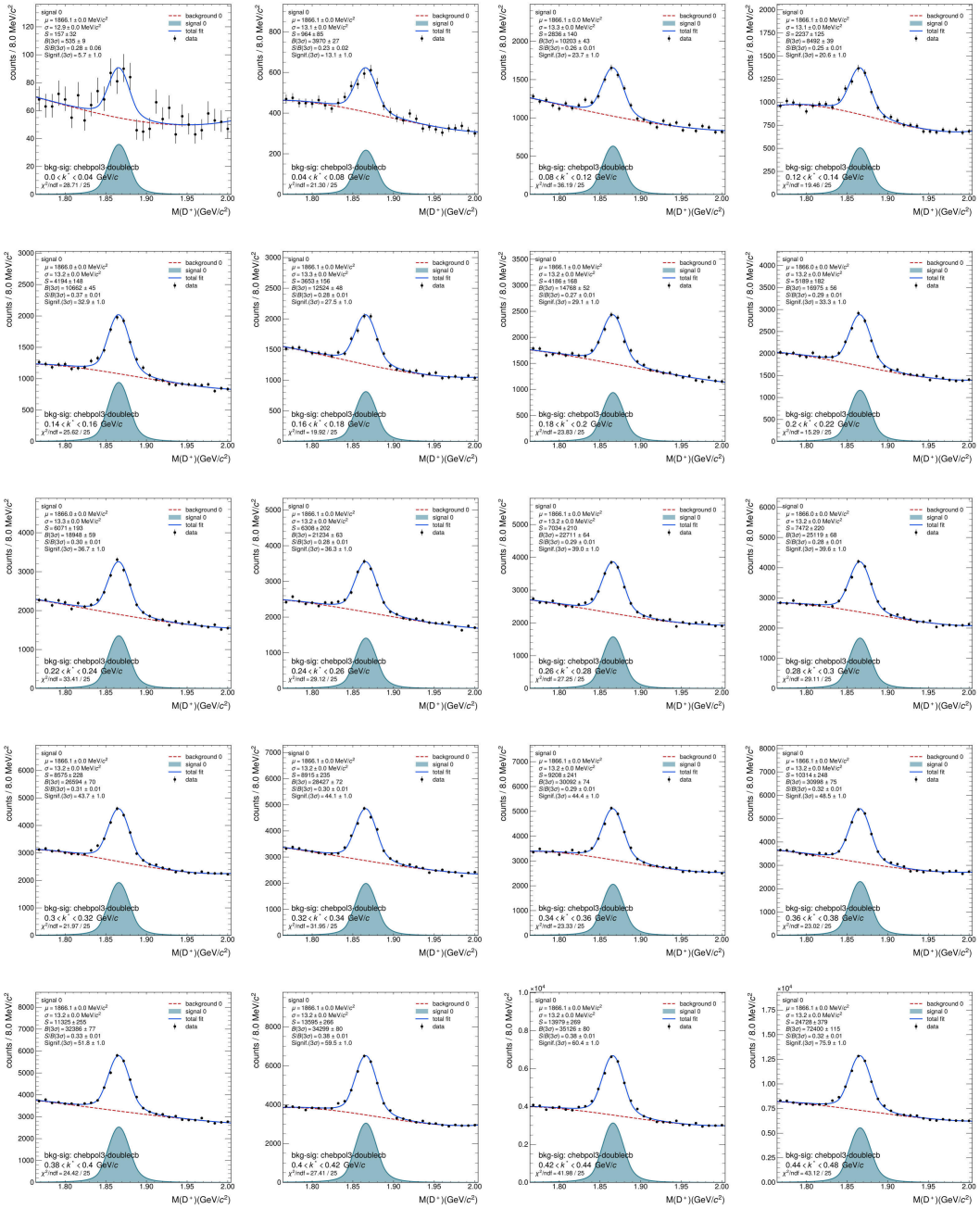

Figure 19: Invariant-mass distribution of D^+ candidates in same-event pairs in the $0 < k^* < 0.48$ GeV/c interval, with the result of the fit (blue line: total, red dashed line: background, cyan line: signal).

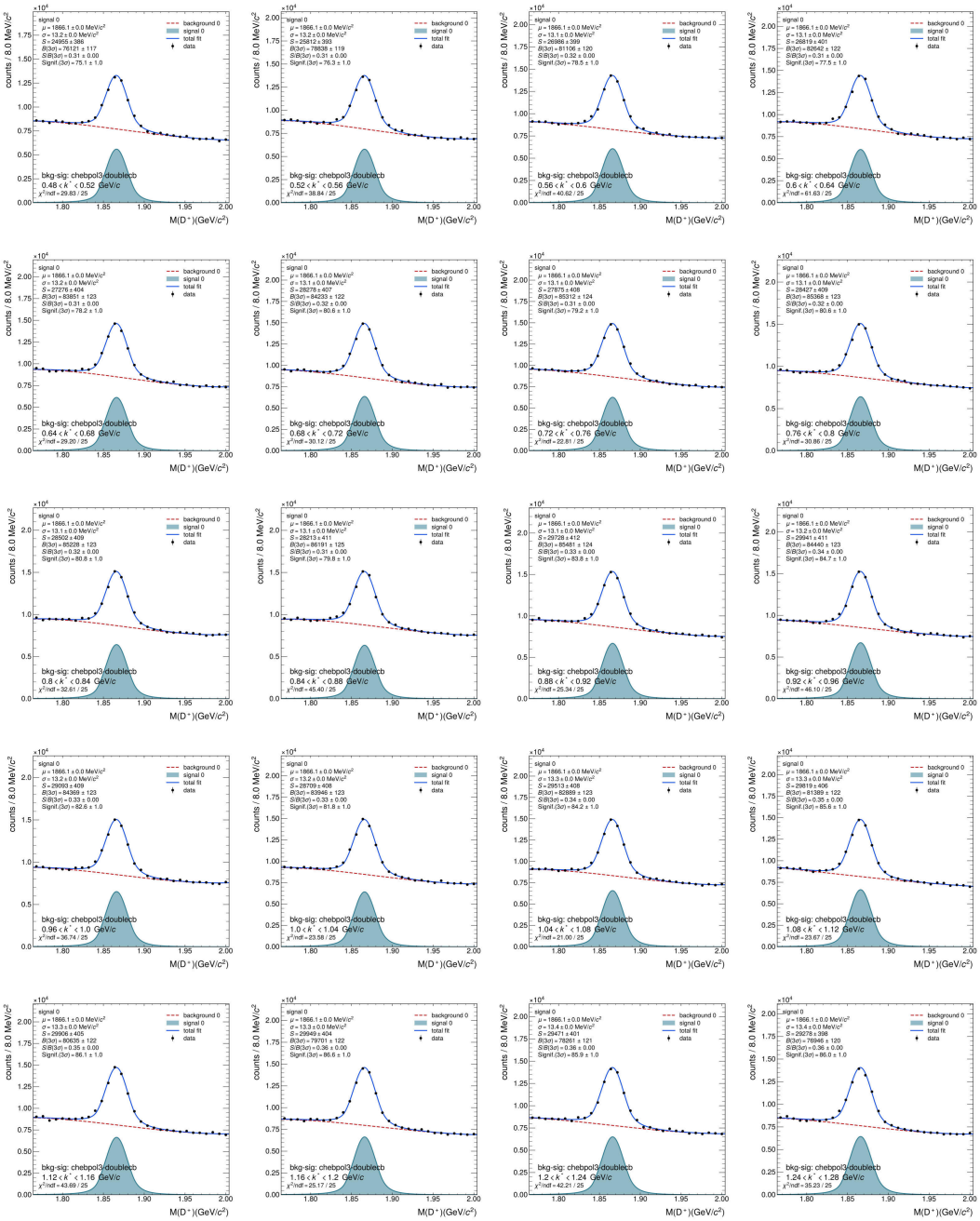

Figure 20: Invariant-mass distribution of D^+ candidates in same-event pairs in the $0.48 < k^* < 1.28$ GeV/c interval, with the result of the fit (blue line: total, red dashed line: background, cyan line: signal).

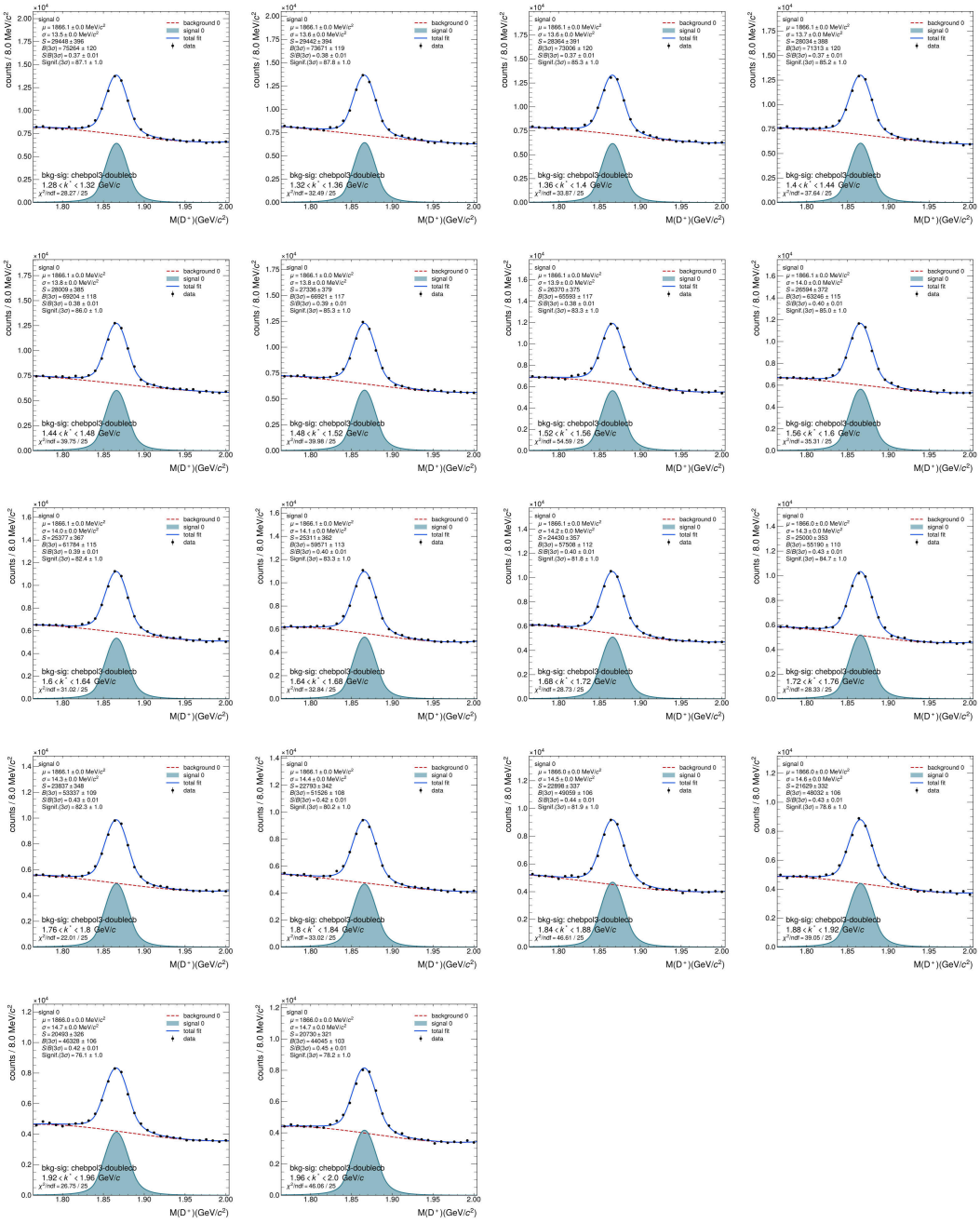

Figure 21: Invariant-mass distribution of D^+ candidates in same-event pairs in the $1.28 < k^* < 2.0$ GeV/c interval, with the result of the fit (blue line: total, red dashed line: background, cyan line: signal).

$M(\mathrm{D}_{s1}(2536)^+) - M(\pi^0) = 2.400$ GeV/c^2, consistent with the PDG masses of the $\mathrm{D}_{s1}(2536)^+$ and of the π^0 [25]. The observation of these two known resonances in the $\mathrm{D}^{\pm}$–K^0_S correlation function demonstrates the feasibility of identifying known resonances in femtoscopic correlation functions of the charm–strange system and provides an important internal cross-check of the analysis.

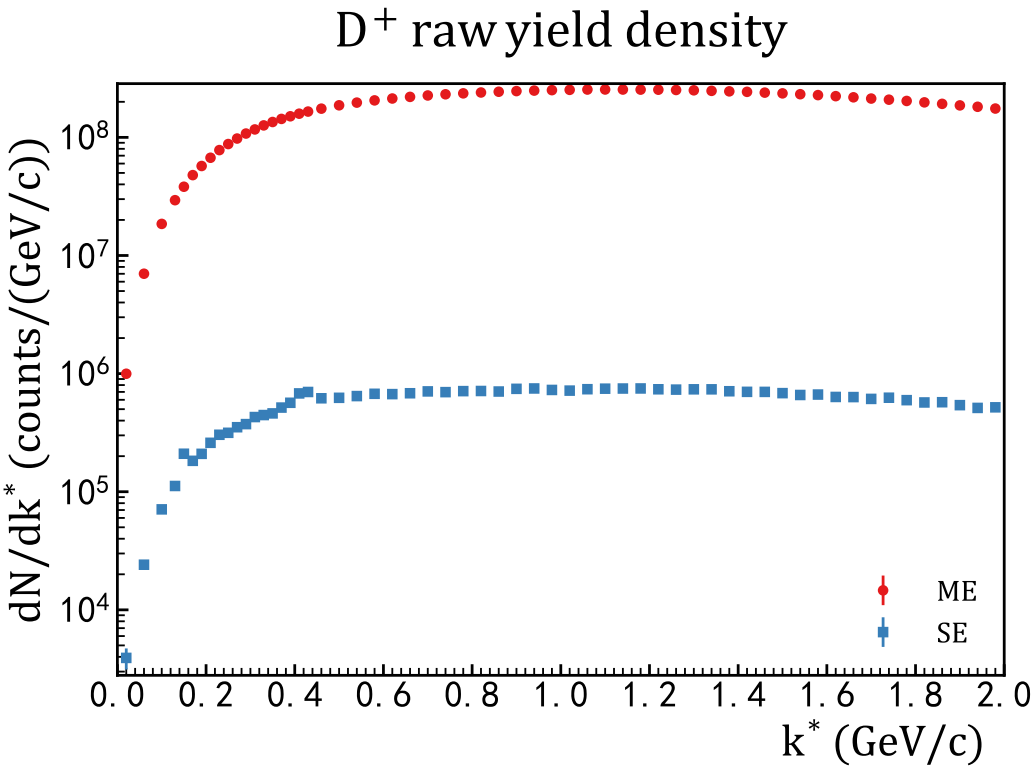

Figure 22: Raw k^* distributions of the merged $\mathrm{D}^{\pm}$–K^0_S pairs for the same-event (SE) and mixed-event (ME) samples.

5.5 Minijet contribution

In pp collisions, a large fraction of the pairs with small relative momentum originates from minijets: clusters of hadrons produced by the fragmentation of partons from semi-hard scatterings, with momentum transfers between the hard and the soft regimes. The hadrons of a minijet are emitted in a collimated cone (small $\Delta\eta$ and $\Delta\phi$) and the corresponding pairs populate preferentially the low-k^* region, largely overlapping with the genuine femtoscopic signal of the short-range $\mathrm{D}^{\pm}$–K^0_S interaction. The minijet contribution is therefore a serious physical background that must be subtracted.

In this analysis, the minijet contribution is evaluated with PYTHIA8 Monte Carlo simulations, using the colour-reconnection mode 2 (CRMode2) tune [34]. The generator records the full production history of each particle, including its parent and its production vertex; this information allows the pairs originating from minijet fragmentation to be tagged in the simulated sample and a pure

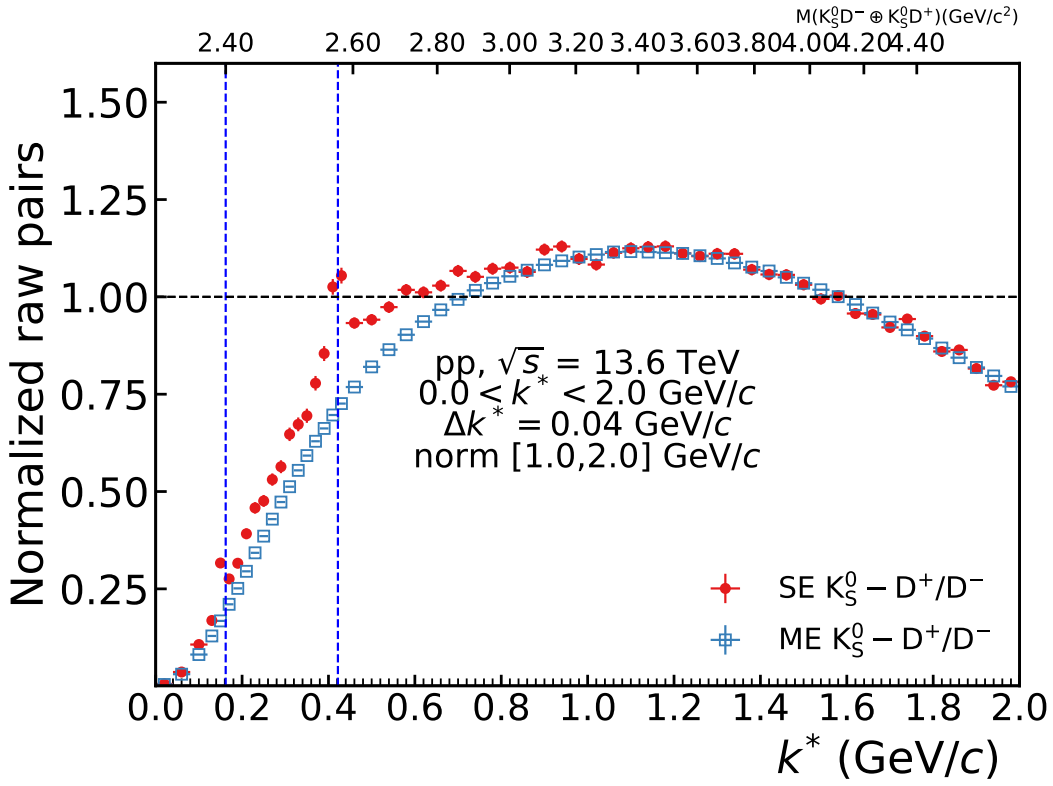

Figure 23: Normalised k^* distributions of the merged $D^{\pm}$–K^0_S pairs for the SE and ME samples, normalised to unity in the $1 < k^* < 2$ GeV/c interval.

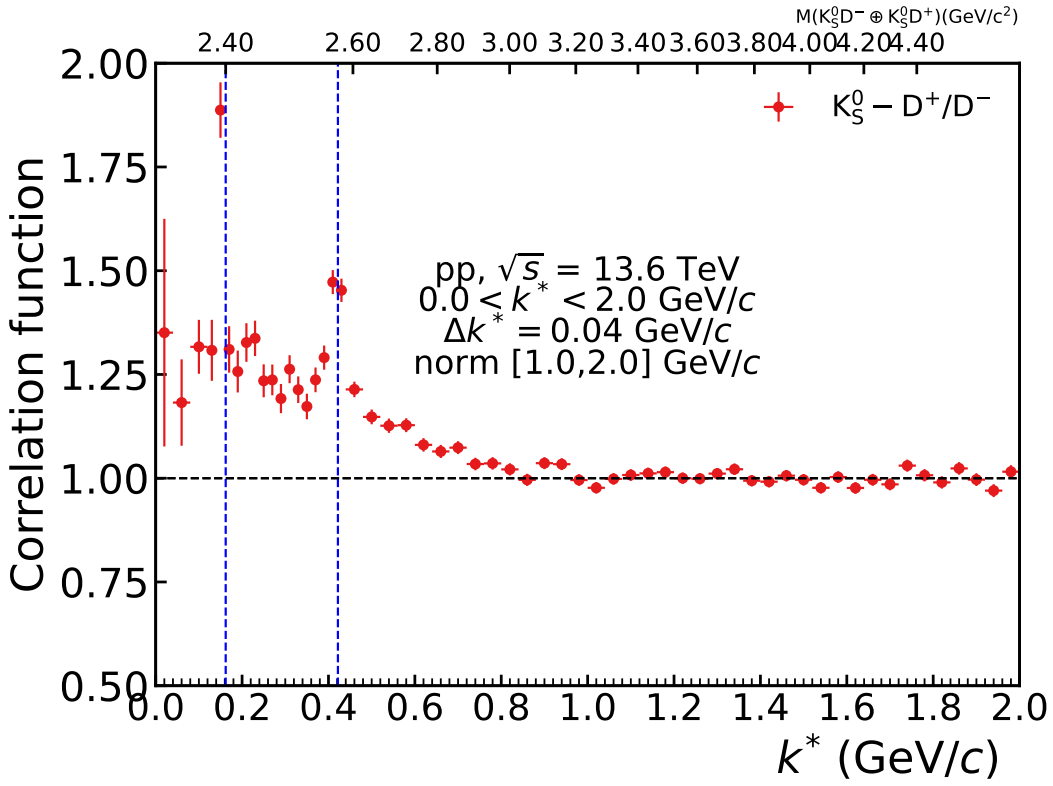

Figure 24: Raw correlation function of the merged $\mathrm{D}^{\pm}$–K^0_S pairs as a function of k^*.

minijet correlation template $C_{\mathrm{mini}}(k^*)$ to be constructed, applying the same kinematic selections and analysis cuts as for the data.

Since PYTHIA does not reproduce the transverse-momentum spectra of the $\mathrm{D}^{\pm}$ and K^0_S with sufficient accuracy, a reweighting procedure is applied to the simulated pairs in order to correct the phase space. First, the p_T distributions of the $\mathrm{D}^{\pm}$ and K^0_S candidates are extracted from data in the same-event (SE) and mixed-event (ME) samples, for each of the four multiplicity intervals used in the analysis. Since the event mixing responds differently in the different multiplicity intervals, the multiplicity distribution of the mixed events is not accurate; moreover, the p_T distributions differ across the intervals. The ME p_T distributions are therefore reweighted to the SE ones,

$$\mathrm{ME}_{\mathrm{weighted}}(p_\mathrm{T}) = \sum_{i=1}^{4} w_i \,\mathrm{ME}_i(p_\mathrm{T}), \qquad w_i = \frac{\int \mathrm{SE}_i(p_\mathrm{T})\,\mathrm{d}p_\mathrm{T}}{\int \mathrm{ME}_i(p_\mathrm{T})\,\mathrm{d}p_\mathrm{T}}, \tag{5}$$

where the index i runs over the multiplicity intervals. The resulting p_T distribution is then used to reweight the p_T of the $\mathrm{D}^{\pm}$ and K^0_S particles in the PYTHIA pairs, thus correcting the simulated phase space. Figures 25 and 26 show the comparison of the normalised SE and ME k^* densities between data and simulation, before and after the reweighting: the reweighting substantially improves the agreement with the data.

The minijet correlation function $C_{\text{mini}}(k^*)$ obtained from the reweighted PYTHIA sample is shown in Fig. 27, for the prompt and non-prompt $\mathrm{D}^{\pm}$ components. The genuine correlation function is then obtained by correcting the raw correlation function measured in data according to

$$C_{\text{corrected}}(k^*) = \frac{C_{\text{raw}}(k^*)}{C_{\text{mini}}(k^*)}, \tag{6}$$

where $C_{\text{mini}}(k^*)$ encodes the minijet-induced background. The corrected correlation function is shown in Fig. 28.

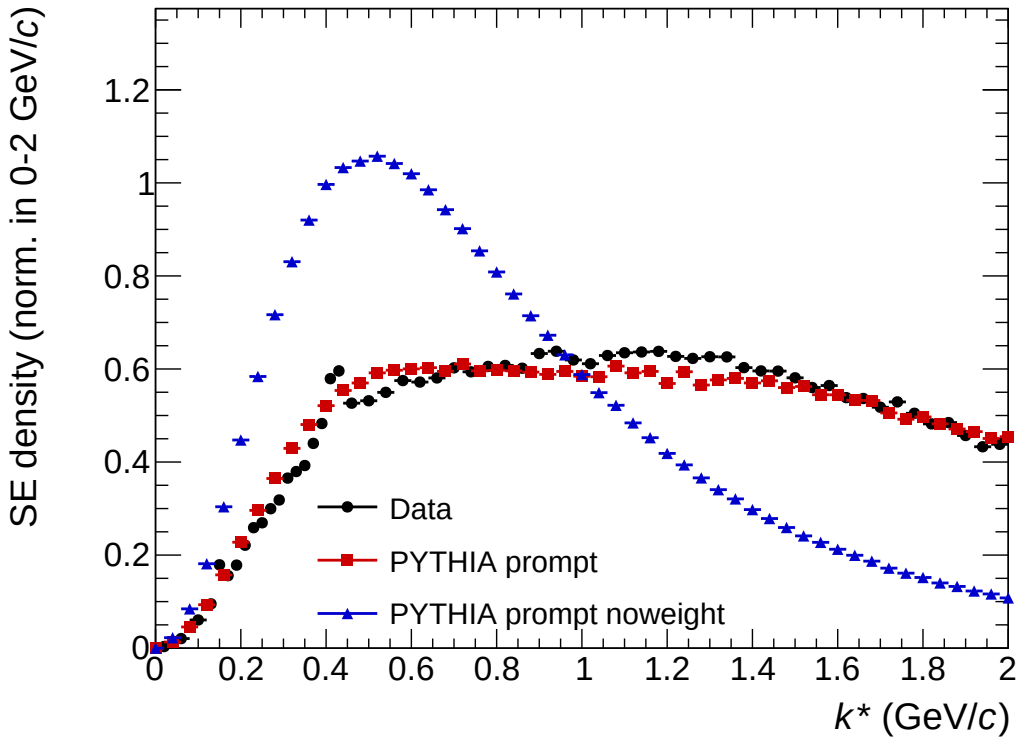

Figure 25: Comparison of the normalised same-event (SE) k^* density between data and the PYTHIA simulation, without and with the p_{T} reweighting.

5.6 Source function

The extraction of the interaction parameters from the measured correlation function requires a precise modeling of the emitting source, which enters the Koonin–Pratt equation, Eq. (1), through the source function $S(\vec{r}^*)$. In this analysis, the source is modelled following the core–halo picture adopted in previous ALICE femtoscopic measurements: a primary Gaussian core, accounting for the directly produced particles, plus a halo contribution from the decays of resonances, which effectively enlarge the source seen by the pairs.

The width of the primary Gaussian core, r_{core}, is obtained from the parametrisation of the transverse-

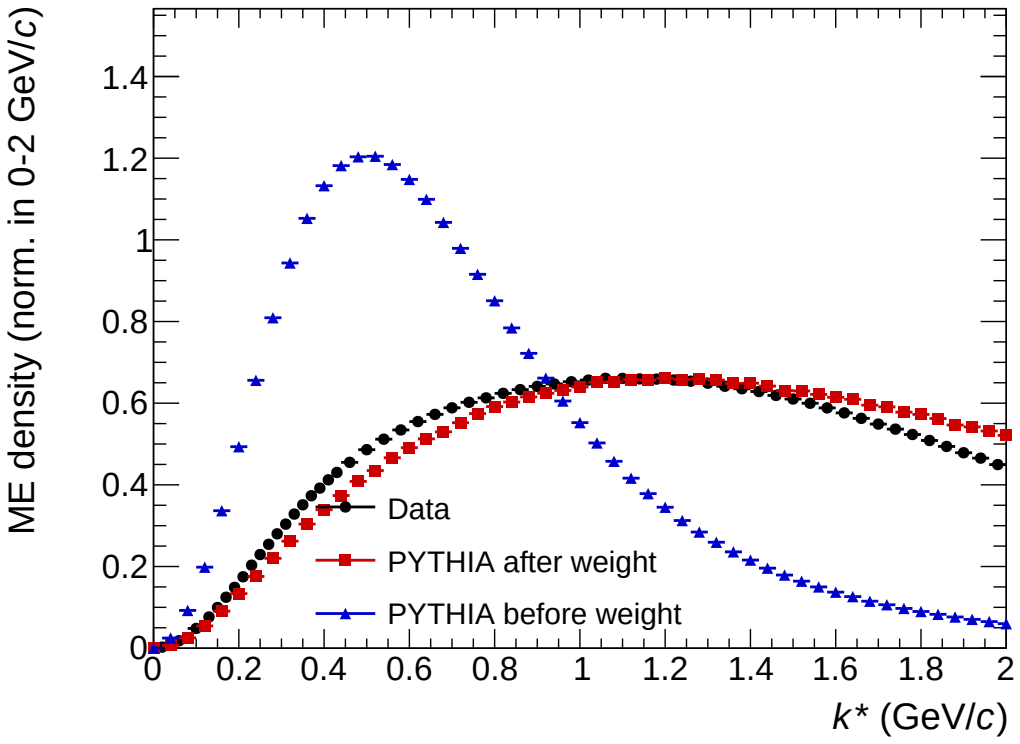

Figure 26: Comparison of the normalised mixed-event (ME) k^* density between data and the PYTHIA simulation, before and after the p_{T} reweighting.

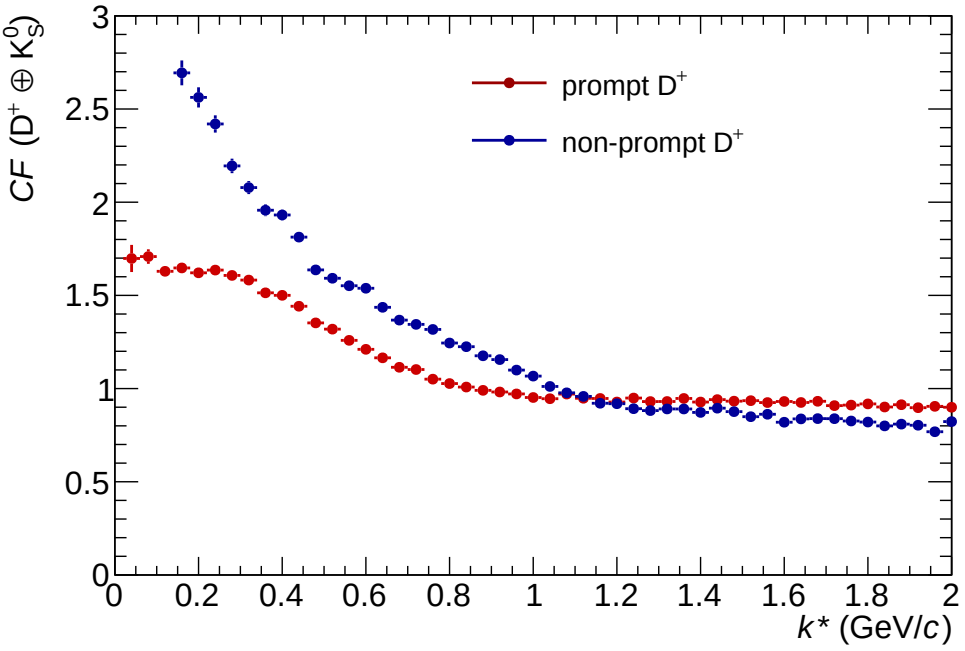

Figure 27: Minijet correlation function $C_{\text{mini}}(k^*)$ from the PYTHIA8 (CR mode 2) simulation after the p_{T} reweighting, for the prompt and non-prompt $\text{D}^{\pm}$ components.

mass dependence of the common hadron emission source, measured by ALICE in different multiplicity intervals [35]. The measured dependence is parametrised as

$$r_{\text{core}} = a \langle m_{\text{T}} \rangle^{b} + c, \tag{7}$$

where the parameters a, b and c depend on the multiplicity interval, and $\langle m_{\text{T}} \rangle$ is the average transverse mass of the pair. For the present analysis, the $\langle m_{\text{T}} \rangle$ distribution of the $\text{D}^{\pm}$–K^0_{S} signal pairs with $k^* < 200$ MeV/c is shown in Fig. 29; the average transverse mass is $\langle m_{\text{T}} \rangle = 2.675$ GeV/c^2. Substituting this value into the parametrisations of the four multiplicity intervals used in the analysis yields $r_{\text{core}} = 0.613$, 0.579, 0.657 and 0.634 fm, which are used as the widths of the primary Gaussian sources.

In addition to the primary core, the decays of resonances contribute to the effective source size, as described by the resonance-source model developed in Refs. [36–39]. In the K^0_{S} sample, a fraction of the candidates originates from the decays of the $K^*(892)^{\pm}$, $K^*(892)^0$ and $\phi(1020)$ resonances, while the D^+ sample receives contributions from the $D_0^*(2400)^+$ and $D_1(2430)^0$ resonances. The corresponding fractions are evaluated, and the source function is computed with Monte Carlo simulations, separating the contributions of the pairs with a resonant $\text{D}^{\pm}$, a resonant K^0_{S}, or both. The effective source function of the $\text{D}^{\pm}$–K^0_{S} pairs is then parametrised with a double-Gaussian fit, and

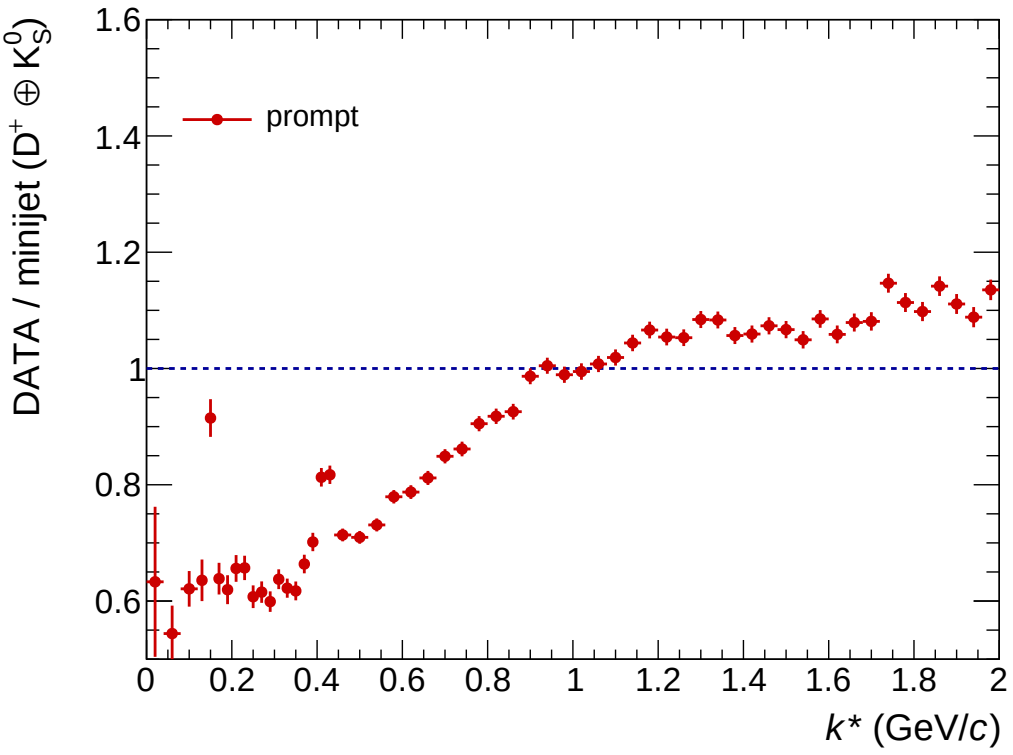

Figure 28: Corrected correlation function of the $D^{\pm}$–K^0_S pairs, obtained as $C_{\text{corrected}}(k^*) = C_{\text{raw}}(k^*)/C_{\text{mini}}(k^*)$ for the prompt component, compared with the PYTHIA minijet template.

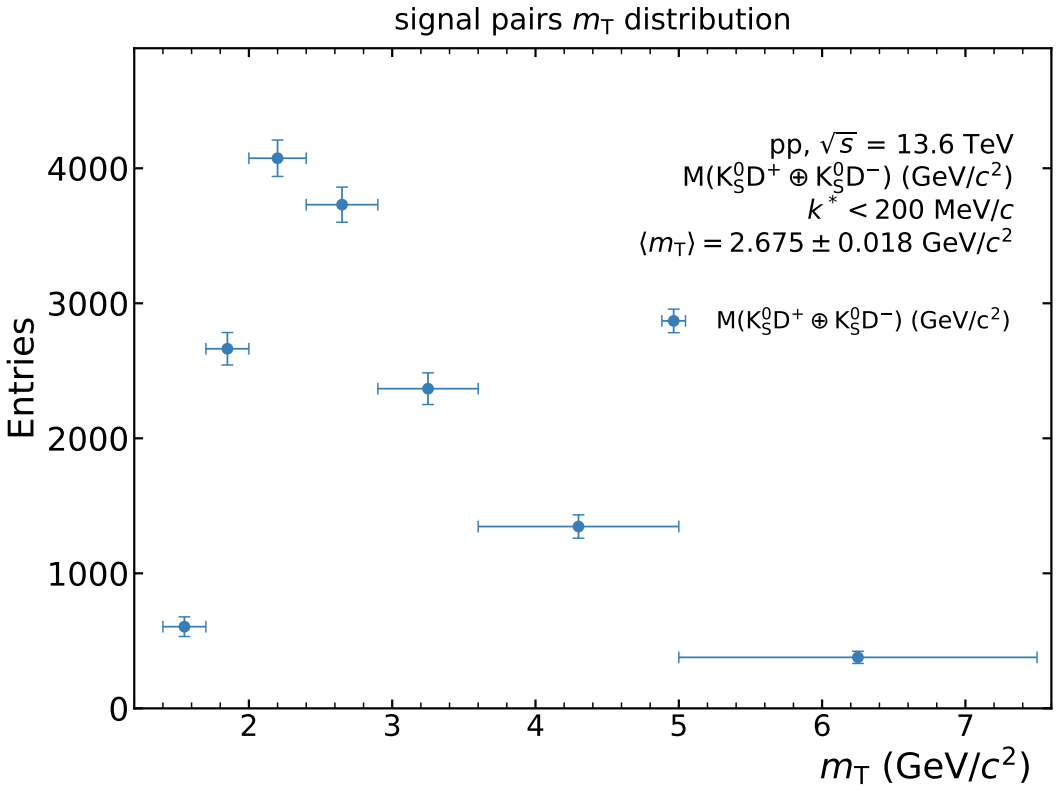

Figure 29: Distribution of the average transverse mass $\langle m_T \rangle$ of the $D^{\pm}$–K^0_S signal pairs with $k^* < 200$ MeV/c; the mean value is 2.675 ± 0.018 GeV/c^2.

the effective source radius r_{eff} is extracted: for the four multiplicity intervals, the merged values are $r_{\text{eff}} = 1.11$, 1.08, 1.14 and 1.13 fm. The effective source functions obtained for the four multiplicity intervals are shown in Figs. 30–33. The resulting source function, together with the solution of the Koonin–Pratt equation, is computed within the CATS (a femtoscopic Correlation Analysis Tool using the Schrödinger equation) framework [33].

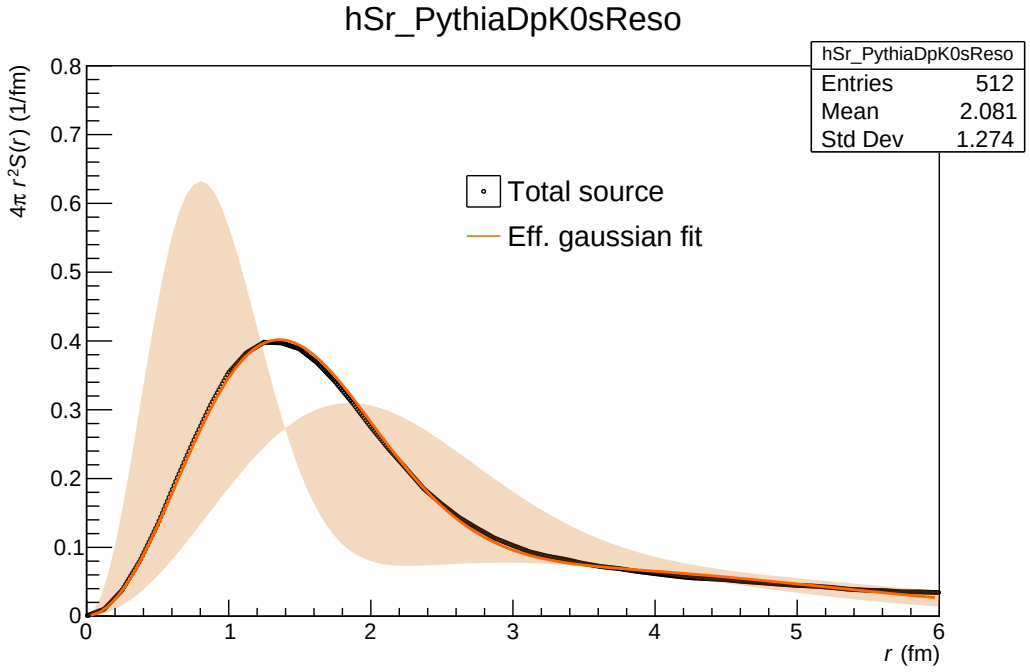

Figure 30: Effective source function $4\pi r^2 S(r)$ of the $\mathrm{D}^{\pm}$–$\mathrm{K}^0_{\mathrm{S}}$ pairs for the multiplicity interval with $r_{\text{core}} = 0.613$ fm, computed with the resonance-source model; the solid curve shows the effective Gaussian fit used to extract r_{eff}.

6 Summary and outlook

In this note, the first measurement of femtoscopic correlations between $\mathrm{D}^{\pm}$ mesons and $\mathrm{K}^0_{\mathrm{S}}$ mesons in pp collisions at $\sqrt{s} = 13.6$ TeV has been presented, using the data collected by ALICE during LHC Run 3 in the 2022 and 2023 data-taking periods. The measurement aims at probing the strong interaction between D and K mesons, providing key experimental input for the determination of the internal structure of the $\mathrm{D}^*_{s0}(2317)$ exotic state.

The $\mathrm{D}^{\pm}$ mesons were reconstructed via the $\mathrm{D}^{\pm} \to \pi^{\pm}\mathrm{K}^{\mp}\pi^{\pm}$ decay channel, applying stringent track-quality and topological preselections followed by a multiclass boosted decision tree based on the XGBoost algorithm, which provides a highly pure prompt $\mathrm{D}^{\pm}$ sample. The $\mathrm{K}^0_{\mathrm{S}}$ mesons were reconstructed via the $\mathrm{K}^0_{\mathrm{S}} \to \pi^+\pi^-$ decay channel exploiting the characteristic V0 topology, with negligible residual background. The correlation functions were constructed with the event-mixing technique, and the pair yields were extracted with per-k^* invariant-mass fits using a double

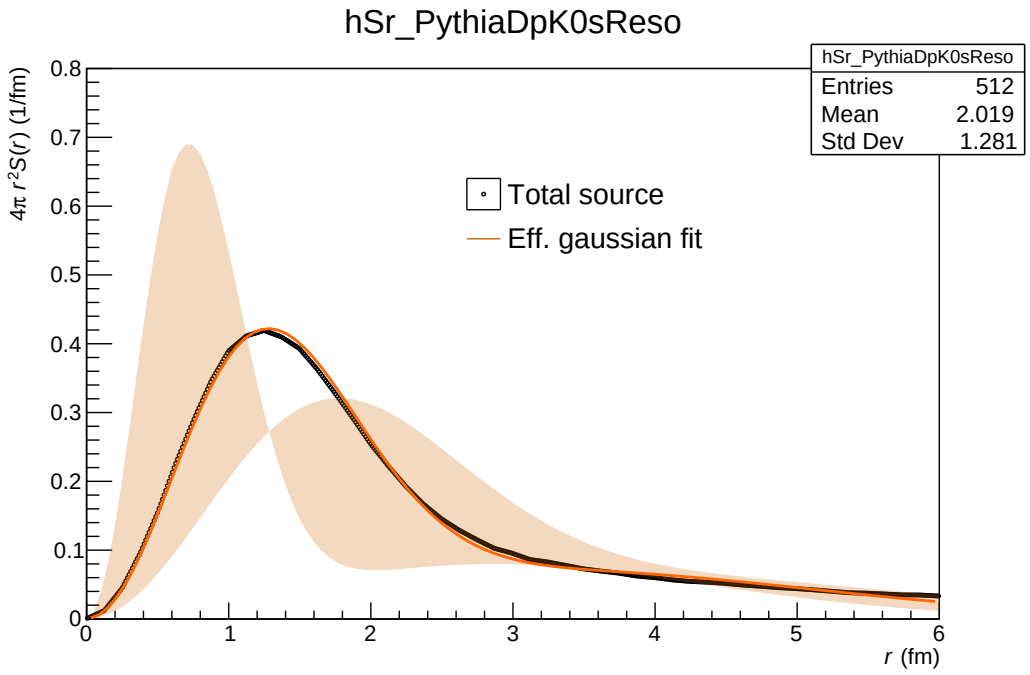

Figure 31: Effective source function $4\pi r^2 S(r)$ of the $\mathrm{D}^{\pm}$–K^0_S pairs for the multiplicity interval with $r_{\mathrm{core}} = 0.579$ fm, computed with the resonance-source model; the solid curve shows the effective Gaussian fit used to extract r_{eff}.

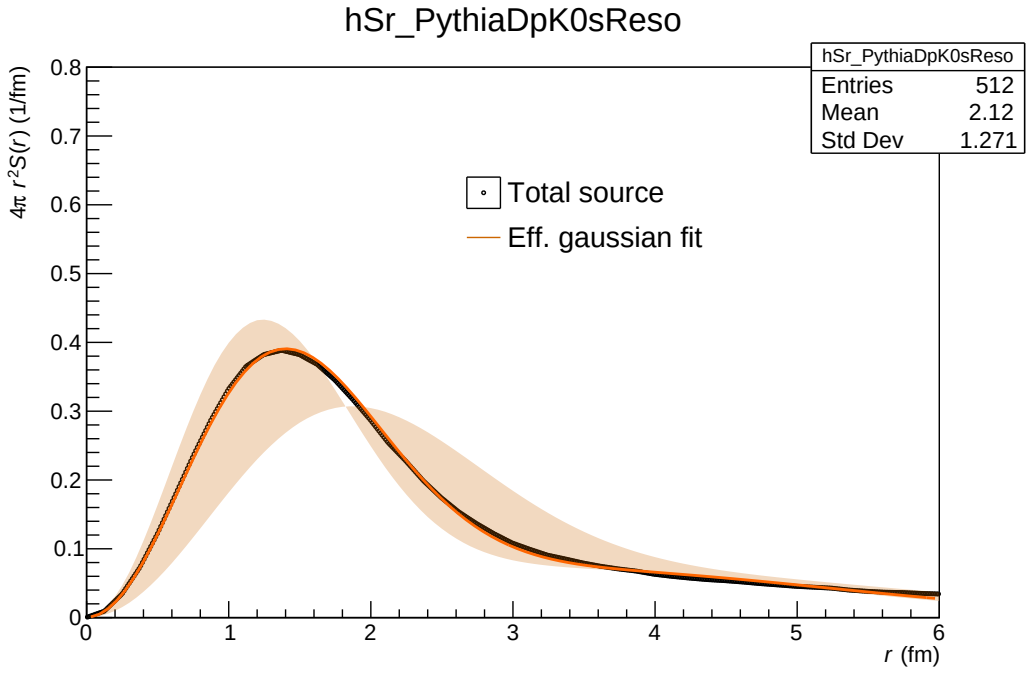

Figure 32: Effective source function $4\pi r^2 S(r)$ of the $\mathrm{D}^{\pm}$–K^0_S pairs for the multiplicity interval with $r_{\mathrm{core}} = 0.634$ fm, computed with the resonance-source model; the solid curve shows the effective Gaussian fit used to extract r_{eff}.

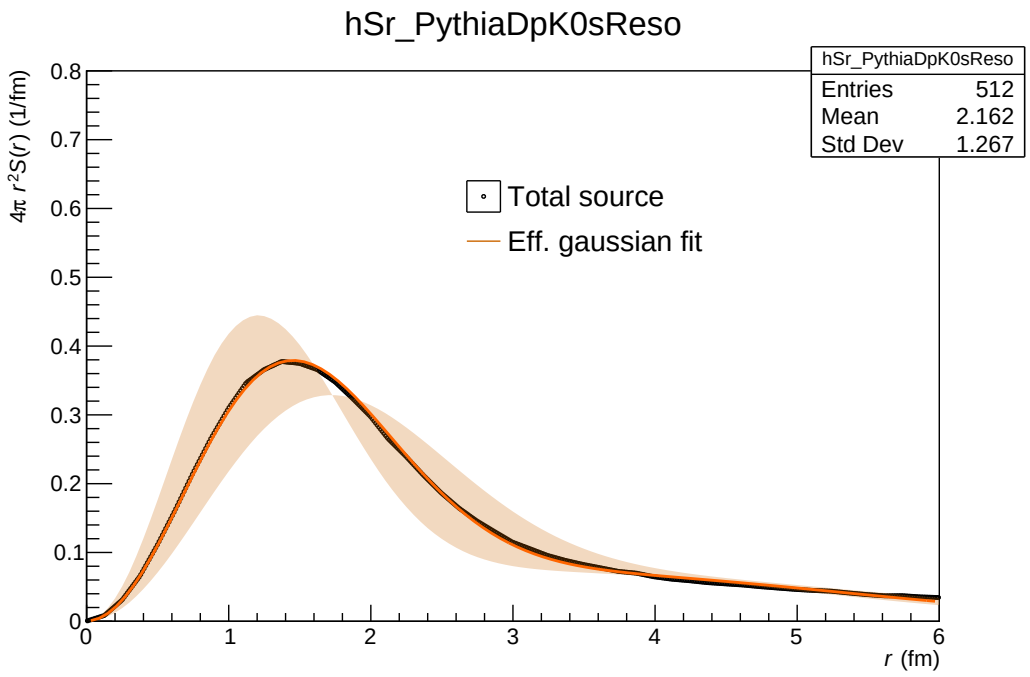

Figure 33: Effective source function $4\pi r^2 S(r)$ of the $\mathrm{D}^{\pm}$–K^0_S pairs for the multiplicity interval with $r_{\mathrm{core}} = 0.657$ fm, computed with the resonance-source model; the solid curve shows the effective Gaussian fit used to extract r_{eff}.

Crystal Ball function for the signal and a Chebyshev polynomial for the combinatorial background. Since the D^+–K^0_S and D^-–K^0_S correlation functions are consistent with each other, the two charge combinations were merged. The minijet background was evaluated with PYTHIA8 simulations and removed from the measured correlation function by a division by the minijet template, after a p_T reweighting procedure that corrects the simulated phase space. The source function of the $\mathrm{D}^{\pm}$–K^0_S pairs was modelled with the core–halo picture, using the r_{core} parametrisation measured by ALICE as a function of the pair transverse mass and accounting for the contribution of resonance decays with the resonance-source model.

Two known resonances were identified in the measured correlation function: the $\mathrm{D}^*_{s2}(2573)^+$, decaying directly into $D^+\mathrm{K}^0_\mathrm{S}$ and visible at $M = 2.569$ GeV/c^2, and the $\mathrm{D}_{s1}(2536)^+$, decaying into $D^{*+}\mathrm{K}^0_\mathrm{S}$ and appearing at $M(\mathrm{D}_{s1}(2536)^+) - M(\pi^0) = 2.400$ GeV/c^2 through the feed-down of the D^{*+}. Their positions agree with the expected masses, and this observation represents the first identification of known resonances in a charm–strange femtoscopic correlation function, providing an important internal cross-check of the analysis. In addition, the measured correlation function exhibits a suppression at low k^*, qualitatively consistent with the prediction of a strongly attractive DK interaction associated with the $\mathrm{D}^*_{s0}(2317)$ molecular picture [19], although the quantitative interpretation requires a full comparison with theoretical models.

Several aspects of the analysis are still in progress or foreseen for the future. The systematic uncertainties of the measurement, including those related to the invariant-mass fitting, the BDT

selections, the non-prompt fraction estimation and the modeling of the minijet background, are under evaluation. The corrected correlation function will be fitted with state-of-the-art theoretical calculations, such as the leading-order chiral-perturbation-theory coupled-channel model of Ref. [19] or the model-independent approach of Ref. [20], to extract the scattering length and the effective range of the DK interaction and to test quantitatively the DK bound-state hypothesis. Since the K^0_S is a superposition of K^0 and $\overline{\mathrm{K}}^0$, a complete theoretical description of the $\mathrm{D}^\pm$–K^0_S correlation function requires coupled-channel calculations accounting for the K^0–$\overline{\mathrm{K}}^0$ mixing. The residual feed-down of the $\mathrm{D}^\pm$ from beauty-hadron decays, quantified by the non-prompt fraction estimated in Section 3, will be accounted for in the comparison with the models. Finally, the analysis will benefit from the larger statistics expected from the ongoing LHC Run 3 data taking, which will allow a finer k^* binning and a more precise measurement of the low-k^* region.

References

[1] H. Fritzsch, M. Gell-Mann, H. Leutwyler, "Advantages of the color octet gluon picture," Phys. Lett. B **47** (1973) 365.

[2] D. J. Gross, F. Wilczek, "Ultraviolet behavior of non-Abelian gauge theories," Phys. Rev. Lett. **30** (1973) 1343.

[3] H. D. Politzer, "Reliable perturbative results for strong interactions?," Phys. Rev. Lett. **30** (1973) 1346.

[4] M. Gell-Mann, "A schematic model of baryons and mesons," Phys. Lett. **8** (1964) 214.

[5] G. Zweig, "An SU(3) model for strong interaction symmetry and its breaking," CERN-TH-401 (1964).

[6] S.-K. Choi *et al.* (Belle Collaboration), "Observation of a narrow charmonium-like state in exclusive $B^\pm \to K^\pm \pi^+ \pi^- J/\psi$ decays," Phys. Rev. Lett. **91** (2003) 262001.

[7] Z. Q. Liu *et al.* (Belle Collaboration), "Study of $e^+e^- \to \pi^+\pi^- J/\psi$ and observation of a charged charmoniumlike state at Belle," Phys. Rev. Lett. **110** (2013) 252002.

[8] B. Aubert *et al.* (BaBar Collaboration), "Observation of a narrow meson state decaying to $D_s^+\pi^0$ at a mass of 2.32 GeV/c^2," Phys. Rev. Lett. **90** (2003) 242001.

[9] R. Aaij *et al.* (LHCb Collaboration), "Observation of a narrow pentaquark state, $P_c(4312)^+$, and of the two-peak structure of the $P_c(4450)^+$," Phys. Rev. Lett. **122** (2019) 242001.

[10] R. Aaij *et al.* (LHCb Collaboration), "Observation of an exotic narrow doubly charmed tetraquark," Nature Phys. **18** (2022) 751.

[11] H.-X. Chen, W. Chen, X. Liu, S.-L. Zhu, "The hidden-charm pentaquark and tetraquark states," Phys. Rept. **639** (2016) 1.

[12] S. E. Koonin, "Proton pictures of high-energy nuclear collisions," Phys. Lett. B **70** (1977) 43.

[13] S. Pratt, T. Csörgő, J. Zimányi, "Detailed predictions for two-proton correlations," Phys. Rev. C **42** (1990) 2646.

[14] M. A. Lisa, S. Pratt, R. Soltz, U. Heinz, "Femtoscopy in relativistic heavy ion collisions," Annu. Rev. Nucl. Part. Sci. **55** (2005) 357.

[15] ALICE Collaboration, "Unveiling the strong interaction among hadrons at the LHC," Nature **588** (2020) 232.

[16] ALICE Collaboration, "Scattering studies with low-energy kaon–proton femtoscopy in proton–proton collisions at the LHC," Phys. Rev. Lett. **124** (2020) 092301.

[17] D. L. Mihaylov (ALICE Collaboration), "First experimental test of HAL QCD lattice calculations for the multi strange hyperon–nucleon interaction with ALICE," Nucl. Phys. A **1005** (2021) 121835.

[18] ALICE Collaboration, "$K^0_S K^0_S$ and $K^0_S K^{\pm}$ femtoscopy in pp collisions at $\sqrt{s} = 5.02$ and 13 TeV," Phys. Lett. B **833** (2022) 137335.

[19] Z.-W. Liu, J.-X. Lu, L.-S. Geng, "Study of the DK interaction with femtoscopic correlation functions," Phys. Rev. D **107** (2023) 074019.

[20] N. Ikeno, G. Toledo, E. Oset, "Model independent analysis of femtoscopic correlation functions: an application to the $D^*_{s0}(2317)$," Phys. Lett. B **847** (2023) 138281.

[21] G. Eulisse, D. Rohr, "The O2 software framework and GPU usage in ALICE online and offline reconstruction in Run 3," EPJ Web Conf. **295** (2024) 05022.

[22] R. Quishpe *et al.*, "Hyperloop – the ALICE analysis train system for Run 3," J. Phys. Conf. Ser. **2438** (2022) 012091.

[23] ALICE Collaboration, "The ALICE experiment upgrades," JINST **17** (2022) P05024.

[24] M. Slupecki (ALICE Collaboration), "Fast Interaction Trigger for ALICE upgrade," Nucl. Instrum. Methods A **1039** (2022) 167021.

[25] R. L. Workman *et al.* (Particle Data Group), "Review of particle physics," Prog. Theor. Exp. Phys. **2022** (2022) 083C01.

[26] T. Chen, C. Guestrin, "XGBoost: a scalable tree boosting system," in *Proceedings of the 22nd ACM SIGKDD International Conference on Knowledge Discovery and Data Mining*, San Francisco, 2016, p. 785.

[27] M. T. Camerlingo *et al.*, "hipe4ml: a machine learning framework for high-energy physics," Comput. Phys. Commun. **293** (2025) 109291.

[28] ALICE Collaboration, "Observation of deuteron and antideuteron formation from resonance-decay nucleons," Nature **648** (2025) 306.

[29] R. Lednický, "Correlation femtoscopy," Nucl. Phys. A **774** (2006) 189.

[30] H. W. Barz, A. Bonasera, S. E. Koonin, "A method for eliminating the background in two-particle correlation measurements," Phys. Lett. B **170** (1986) 15.

[31] J. E. Gaiser, "Charmonium spectroscopy from radiative decays of J/ψ, ψ' and ψ''," Ph.D. thesis, Stanford University, SLAC-R-255 (1982).

[32] ALICE Collaboration, "Measurement of beauty and charm production in pp collisions at $\sqrt{s} =$ 5.02 TeV via non-prompt and prompt D mesons," JHEP **05** (2021) 220.

[33] D. L. Mihaylov, V. Mantovani Sarti, O. W. Arnold, L. Fabbietti, B. Mormone, "A femtoscopic Correlation Analysis Tool using the Schrödinger equation (CATS)," Eur. Phys. J. C **78** (2018) 394.

[34] T. Sjöstrand *et al.*, "An introduction to PYTHIA 8.2," Comput. Phys. Commun. **191** (2015) 159.

[35] ALICE Collaboration, "Multiplicity dependence of the size of the common hadron emission source in pp collisions at the LHC," arXiv:2606.28098 [nucl-ex].

[36] ALICE Collaboration, "Search for a common baryon source in high-multiplicity pp collisions at the LHC," Phys. Lett. B **811** (2020) 135849.

[37] ALICE Collaboration, "Corrigendum to 'Search for a common baryon source in high-multiplicity pp collisions at the LHC' [Phys. Lett. B 811 (2020) 135849]," Phys. Lett. B **861** (2025) 139233.

[38] ALICE Collaboration, "Common femtoscopic hadron-emission source in pp collisions at the LHC," Eur. Phys. J. C **85** (2025) 198.

[39] ALICE Collaboration, "Investigating the p-$\pi^{\pm}$ and p-p-$\pi^{\pm}$ dynamics with femtoscopy in pp collisions at $\sqrt{s} = 13$ TeV," arXiv:2502.20200 [nucl-ex].